

Wright State University

CORE Scholar

[Browse all Theses and Dissertations](#)

[Theses and Dissertations](#)

2014

Finite Element Simulation of Skull Fracture Evoked by Fall Injuries

Anthony Vicini

Wright State University

Follow this and additional works at: https://corescholar.libraries.wright.edu/etd_all



Part of the [Biomedical Engineering and Bioengineering Commons](#)

Repository Citation

Vicini, Anthony, "Finite Element Simulation of Skull Fracture Evoked by Fall Injuries" (2014). *Browse all Theses and Dissertations*. 1274.

https://corescholar.libraries.wright.edu/etd_all/1274

This Thesis is brought to you for free and open access by the Theses and Dissertations at CORE Scholar. It has been accepted for inclusion in Browse all Theses and Dissertations by an authorized administrator of CORE Scholar. For more information, please contact library-corescholar@wright.edu.

FINITE ELEMENT SIMULATION OF SKULL
FRACTURE EVOKED BY FALL
INJURIES

A thesis submitted in partial fulfillment of the
requirements for the degree of
Master of Science in Engineering

By

Anthony Vicini

B.S., Case Western University, 2012

2015

Wright State University

WRIGHT STATE UNIVERSITY
GRADUATE SCHOOL

December 8, 2014

I HEREBY RECOMMEND THAT THE THESIS PREPARED UNDER
MY SUPERVISION BY Anthony Vicini ENTITLED Finite Element
Simulation of Skull Fracture Evoked by Fall Injuries BE ACCEPTED IN
PARTIAL FUFILLMENT OF THE REQUIREMENTS FOR THE
DEGREE OF Master of Science in Engineering

Tarun Goswami, D.Sc.
Thesis Director

Committee on
Final Examination

Thomas N Hangartner, Ph.D.
Department Chair

Nasser H Kashou, Ph.D.

Mary Fendley, Ph.D.

David Reynolds, Ph.D.

Robert E. W. Fyffe, Ph.D.

Vice President for Research and
Dean of the Graduate School

ABSTRACT

Vicini, Anthony. M.S.Egr. Department of Biomedical, Industrial & Human Factors Engineering, Wright State University, 2015. Finite Element Simulation of Skull Fracture Evoked by Fall Injuries.

This study presents novel predictive equations for von Mises stresses and deflection of bones in the frontal and lateral regions of the skull. The equations were developed based on results of a finite element model developed here. The model was validated for frontal and lateral loading conditions with input values mimetic to fall scenarios. Using neural network processing of the information derived from the model achieved R^2 values of 0.9990 for both the stress and deflection. Based on the outcome of the fall victims, a threshold von Mises stress of 40.9 to 46.6 MPa was found to indicate skull fracture given a maximum input force of 26 kN and a load rate of 40 kN/ms.

Table of Contents

1. Introduction.....	1
1.1. Formation of Traumatic Brain Injury	1
1.1.1. Diffuse Axonal Injury (DAI)	1
1.1.2. Hematoma	3
1.1.3. Skull Fracture.....	3
1.2. Causes of TBI	4
1.2.1. Falls.....	5
1.2.2. Motor Vehicular Collision	6
1.2.3. Sports	6
1.2.4. Blast Wave Neurotrama	7
2. Review of Literature	8
2.1. Human Testing.....	8
2.2. Animal Testing.....	11
2.3. Finite Element Modeling	13
2.4. Predictive Models	17
3. Computational Sensitivity Analysis of Fracture Thresholds in Literature	23
4. Computational Materials and Methods	28
4.1. Source Image CT details	28
4.2. Meshing.....	29

4.3. Viscoelastic modeling	30
4.4. Force modeling	32
4.5. Boundary Conditions	35
5. Results of Finite Element Analysis	37
5.1. Von Mises Stress Analysis	38
5.2. Displacement Values	41
6. Discussion	43
6.1. Least Squares Analysis of the Effect of Maximum Load on Maximum Stress	44
6.2. Least Squares Analysis of the Effect of Load Rate on Maximum Stress	45
6.3. Least Squares Analysis of the Effect of Strike Location on Maximum Stress	47
6.4. Least Squares Analysis of the Effect of Combination Terms on Maximum Stress	49
6.5. Least Squares Prediction Equation for Stress Values	51
6.6. Neural Network Analysis for Stress in the Skull	54
6.7. Maximum Displacement	59
6.8. Least Squares Analysis of the Effect of Maximum Load on Displacement	60
6.9. Least Squares Analysis of the Effect of Load Rate on Displacement	61
6.10. Least Squares Analysis of the Effect of Strike Location on Displacement	63

6.11.Least Squares Analysis of the Effect of Combination Terms on Displacement.....	65
6.12.Least Squares Prediction Equation for Displacement.....	66
6.13.Neural Network Analysis for Displacement in the Skull.....	68
6.14.Comparison of Results	73
7. Conclusions.....	74
8. References.....	76

Table of Figures

Figure	Page
1) Damaged neurons due to impact.....	12
2) Injury threshold based on strain rate.....	14
3) DAI and hematoma tolerance curves.....	15
4) Strain on corpus callosum.....	17
5) Fracture risk curve developed by Cormier.....	21
6) Selected fracture forces for lateral and frontal impacts	23
7) Neural predictive model for frontal impacts based on literature data.....	24
8) Sensitivity analysis of literature based neural model.....	26
9) CT images of skull used herein.....	28
10) Maxwell-Wiechert viscoelastic model.....	29
11) Force locations with respect to anatomical landmarks	31
12) Representative force curves from fall events.....	33
13) Representative transformed force curves used in simulation	34
14) Force and boundary conditions from a simulation	36
15) Distribution of stress values from a simulation	37
16) Stress and displacement over time maximum stress element	38
17) Distribution of maximum stress values.....	39
18) Distribution of displacement values.....	41
19) Leverage of load on stress.....	44
20) Box plot of load on stress.....	44
21) Leverage of load rate on stress.....	45

22) Box plot of load rate on stress.....	46
23) Leverage plot of location on stress	47
24) Box plot of location on stress.....	48
25) Leverage test of other variables on stress	49
26) Relative influence of variables on stress.....	50
27) Graph of stress based on least squares analysis	52
28) Residuals of least squares on force	53
29) Mechanism of neural network	55
30) Contour plot of maximum stress.....	56
31) Effect of load rate on each load value for stress	57
32) Residuals of neural network for stress	58
33) Leverage test of load on displacement.....	60
34) Box plot of load on displacement	60
35) Leverage of load rate on displacement	61
36) Box plot of load rate on displacement	62
37) Leverage of location on displacement	63
38) Box plot of location on displacement	63
39) Leverage plots of other variable son displacement.....	64
40) Relative influence of variables on displacement	65
41) Graph of displacement based on least squares analysis.....	68
42) Residuals of least squares for displacement.....	68
43) Contour plot for neural network of displacement	69
44) Effect of load rate on each load value for displacement.....	72

45) Residuals of neural network for displacement.....	72
---	----

Table of Figures

Tables	Page
1) Head injury scale comparison chart.....	19
2) List of maximum stress values.....	40
3) List of maximum displacement values	42

Table of Equations

Equation	Page
1) Least squares model based on literature data.....	24
2) Neural model based on literature	25
3) Polynomial approximation to force curves	34
4) Least squares equation for maximum stress	52
5) Simplified least squares equation for maximum stress.....	54
6) Neural network model of maximum stress	55
7) Least squares equation for displacement	67
8) Simplified least squares equation for displacement.....	67
9) Neural network model of displacement	70

ACKNOWLEDGEMENTS AND DEDICATION

I would like to make all of those that made this paper possible. Many deserve a place in this section, but I would like to mention a few names in particular. I would like to thank my parents primarily, John and Donna, for their support of higher education. I would like to thank my fellow graduate student, Dinesh Gundapaneni, who instructed me in the usage of software critical to the construction of this thesis. I would also like to thank my advisor, Tarun Goswami for the encouragement, instruction, and support in this journey. Finally, I would like to thank the field of science as a whole: *nanos gigantum humeris insidentes*.

Chapter 1: Introduction

1.1 Formation of Traumatic Brain Injury

Several modes of injury exist in the general term of “traumatic brain injury” (TBI). While the term is usually used to refer specifically to brain damage, skull fracture is almost always lumped into the category. Skull fractures do not always directly pose a risk for brain injury, although the conditions that cause them to form do. These conditions also lead to the formation of life threatening conditions including hematoma or damage to the nerves of the brain due to the extreme conditions imposed upon the soft tissue. Additionally, some modes of skull fracture, such as depressed fractures, can put direct pressure on the brain, causing significant brain damage.

1.1.1 Diffuse Axonal Injury (DAI)

DAI is a condition where the axons of neurons tear, which causes them to lose functionality. DAI is typically caused by shearing forces in the head due to sudden decelerations or rotation. This can happen by means of physical shearing in the case of sufficiently large forces, but lesser forces can lead to biological termination of the neurons. These forces are commonly generated in collisions, and as such, DAI is believed to be the primary mechanism of brain injury for impacts in sports such as football and soccer, and the primary injury mechanism and cause of death for motor vehicle accidents.^{2, 39} Axons that experience forces not sufficient to cause physical interference

with their functionality can instead emit reactive oxygen species. These compounds, which were found to be in abundance following head injury, combine with nitric oxide to form peroxinitrite, which is highly reactive and can cause cell death.⁵ This leads to dysfunction of the axons outside of the immediate time frame of the injury moment, delaying the symptoms of DAI. It is very important therefore, that the physician is able to detect early warning signs for DAI, to know if a patient is at risk and to take the appropriate steps to minimize damage. While there are numerous drug therapies in experimentation to prevent cell death from the oxidative degradation process, such treatments are not in effect for clinical use.

DAI can be classified into multiple tiers, and there are multiple criteria to determine the severity of the injury. One of the most commonly used schemes places DAI into three tiers.¹ Tier 1 injuries will show histological evidence of axonal injury in the white matter of the cerebral hemispheres. Tier 2 injuries are similar, but also show a focal lesion in the corpus callosum. In tier 3 injuries a focal lesion is also present in the dorsolateral quadrant or quadrants of the rostral brain stem. This shows a property of DAI that is counterintuitive to its name. Diffuse axonal injury often results in distinct spots of injury rather than injury across the entire brain. This is believed, in part, to be due to the shearing effects across the boundaries of different parts of the brain, each with different material properties. The shearing experienced by unequal movement of the brain tissue strains the connections there, causing focal injuries, despite the originating force deriving from a uniform, albeit rotating field.

1.1.2. Hematoma

Hematomas can occur from forces that cause the blood vessels, especially the bridging veins closer to the skull, to rupture. When in the brain, hematomas exist in three main forms – epidural, subdural, and intracerebral, which are defined by their location. Epidural hematomas place the fracture between the inside of the skull and the dura mater. Subdural hematomas are between the surface of the brain and the dura, and can often go unnoticed as blood slowly pools into the brain. Intracerebral hematomas take place within the brain tissue itself. Whatever the point of origin, hematoma formation usually results from acceleration of the head. Such a rotation can cause a disparate amount of movement in the skull compared to the brain, stressing and tearing the vessels that are linked from the brain to the skull. The blood from these veins pools within the cranial cavity and displaces the brain. The pressure exerted by the extravasated blood can cause damage to the brain tissues. Typically, a more energetic the collision leads to a greater the number of veins that will be ruptured, which corresponds with an increased speed of blood pooling and pressure development upon the brain. Like DAI, the symptoms of a hematoma can go unnoticed at first. Confusion, drowsiness, and nausea are all symptoms of subdural hematomas – symptoms which could easily be attributed to shock surrounding a traumatic incident.

1.1.3. Skull Fracture

While TBI can occur at thresholds lower than those needed to cause skull fracture, fractures are often lumped into the general category of “traumatic brain injury” and, depending on the nature of the fracture, can indicate for the presence of, or indeed, the

severity of any brain damage.^{4, 8, 9} Skull fracture's likelihood varies based on the location struck, due to the varying thicknesses and orientations of the bone. Additionally, the cranial sutures represent vulnerabilities in the skull's structural integrity. These sutures are composed of fibrous elements and, while they can absorb as much as 5 times the energy per unit volume before failure as bone, they have a lower overall bending strength.²⁹ These represent zones of weakness in the skull, which can lead to structural failure of the cranial cavity at forces lower than would otherwise be indicated by the brain.

The exact variety of fracture depends on the intensity, location, and other factors relating to the blow. In higher energy collisions, direct bending of the bony structure of the skull can result in fracture by strains directly from the impact, forming a depressed fracture. Linear fractures are able to develop outside of the primary strike area however, due to the elastic nature of bone tissue and outbending that develops secondary to the strike.²¹ Linear skull fractures by themselves do not tend to provide complicating factors to an injury, but depressed fractures can physically press upon the brain, causing further damage.²⁶

1.2. Causes of TBI

Likely TBI causes vary based on a subjects age and employment. Common civilian causes include falls, motor vehicle accidents, assault, and sports. For soldiers in combat, explosives in the form of improvised explosive devices produce the majority of head injury due to the pressure wave accompanying them.^{17, 27} Age increases the

probability of injury due to falls, with an estimated one in three people over the age of 65 experiencing at least one fall per year. Due to the surroundings of each injury circumstances, each injury mechanism typically has a slightly different presentation of injury.

1.2.1. Falls

Falls are the most common cause of TBI, accounting for about a third of all cases.¹¹ Fall-induced TBI death rate for persons 80 years and older increased to 38.1 per 100,000 persons despite an increase in the self-reported average health of the age group.⁵⁴ Typically, falls consist of blunt impacts due to the head striking the ground, although depressed or penetrating injuries can occur from hitting a corner such as the edge of a sidewalk or a table. Though they are often at lower energy compared to a motor vehicle collision, falls can cause skull fracture due to the potential energy release of a fall.¹⁹ This is often accentuated as many falls happen in stairwells, where multiple impacts are possible. Fall injuries most often appear in either single or multiple impacts around the “hat brim area,” a 3 cm thickness region around the head with a lower limit formed from the circle connecting the top of the eyebrows to the occipital pole.³¹ Assault, especially in abuse cases, can also present with similar symptoms, although some research has shown the assault injuries tend to occur on the left side of the skull. Complicating this, autopsy reports of those that have died from assaults are unable to determine if the injuries caused in these instances are due to the punching, falls, or other aspects of an assault.²⁰

1.2.2. Motor Vehicular Collision

Compared to falls, motor vehicle collisions can achieve much higher impact energies and cause more fatalities.¹¹ Due to advances in safety devices including airbags, many injuries are at least partially mitigated; however brain injury and skull fracture can occur. Frontal and rear impacts are more associated with soft tissue trauma due to airbags housed in the steering column.^{58, 65} In the event of airbag failure, strikes to the steering wheel can cause fracture as well, even at relatively low velocities.⁶² Similarly, side impacts can evoke head trauma when the head strikes the window. Side airbags help prevent injury, as with their frontal counterpart, but are not standard for all models. This is cause for concern as the skull and brain are more sensitive to impact from the sides for several impact modes in addition to the fact that there is less material from the vehicle to dissipate a blow to the driver's side when compared to strikes from other directions.⁴⁹

1.2.3. Sports

Sports such as football and soccer are troubled with head impacts with over 350 football player deaths since 1945 due to subdural hematomas alone.¹⁶ This is partially due to the inability of football helmets to stop rotational accelerations due to a collision from reaching the brain. Combining that with the up to 1440 head impacts per year received by an NCAA defensive line football player, with about 280 of the hits to the more sensitive lateral areas of the head, and a maximum force of impact that lies near the maximum tolerance of the brain to injury, and it is little wonder that TBI is not uncommon in such sports.^{12, 16}

1.2.4. Blast Wave Neurotrauma

Blast related TBI, found most commonly in IED related injuries imposed upon military populations, is perhaps the most complicated injury format. Primary blast neurotrauma is due to the pressure wave formation of an explosive device. It was found that this traveling pressure wave was amplified while traveling under the helmet and caused ripples in the skull that amplified the damage done by the wave.^{34, 40, 47, 64} In conjunction to this, explosive devices almost always create a cloud of shrapnel, either by the design of the device, or as a result of loose debris in the blast. This debris creates secondary trauma to the body, as well as the possibility of penetrating head injury. In a study of 63 US military personnel with TBI ranging from mild to severe as a result of IED devices, not a single one presented with blast injuries that were not complicated with additional sources of injury.³⁶ Because of this, it is very hard to accurately model a realistic blast injury as no single model can accurately predict the secondary effects of an explosive event.

Though TBI exists in a myriad of forms, all can be life threatening. Falls, vehicular collisions, sports, and assault all involve impacts that can exceed injury thresholds. Symptoms for TBI may not develop until hours after an injury event, so rapid diagnosis and treatment is needed to curb its effects. Skull fracture is the most noticeable symptom, as even smaller fractures can easily be seen on an x-ray. Additionally, because skull fracture is accepted to be linked with more advanced versions of brain injury, it is an excellent indicator of brain injury.

Chapter 2: Review of Literature

In an effort to understand TBI, it is important to construct models of the head. Because of the obvious ethical issue involved, the only human experimentation protocols must be well below levels that could cause injury to the patient. Other sources of limited information can be found in the study of cadavers died after sustaining TBI. Generally, the two sources of models other than sub-injury human testing are by means of animals and finite element models.

2.1. Human testing

Generally, sub-injury level human testing is performed by means of diffusion tensor MRI imaging in order to be able to rapidly measure the response of the brain after an impact is made. In one example of this, the head of a supine patient was dropped such that the back of the head struck upon a padded surface. This test generated a profile of strain for the brain for time points of 18, 78, 84, 90, and 114 milliseconds post impact. Peak accelerations of the runs varied between $21.1 \pm 2.9 \text{ m*s}^{-2}$ and $32.5 \pm 3.2 \text{ m*s}^{-2}$, and essentially no strain values greater than 0.07 m*m^{-1} were seen.⁷ In a similar study, where the patient lay in a prone position, the front of the head was dropped upon padding. Peak translational and rotational accelerations were measured for the brain to be $14.3\text{-}16.3 \text{ m*s}^{-2}$ and $124\text{-}143 \text{ rad*s}^{-2}$ respectively. Similar maximum strains of $0.05\text{-}0.07 \text{ m/m}$ were found.¹⁴ While these values give a reference point for model creation, little

information is gleaned from studies like this in terms of injury prediction thresholds without grievous amounts of extrapolation.

In order to get more practical insights into injury formation, cadavers can be used; however these are in limited supply. In a study in 2011, acoustic sensors were attached to the skull to detect the breaking point for the frontal skull. The skulls were rigidly attached at the occipital lobe to prevent movement and the flat surface of a 6.45 cm, 3.2 kg cylindrical impactor was allowed to fall onto the frontal bone. Analysis of the precise area of impact by means of film in the impacting area allowed for precise calculation of the force experienced by the bone. The study found a 50% risk value for frontal bone fracture at forces for this impactor at values between 1885 and 2405 N, although it was noted that patients with larger frontal sinus cavities showed a greater proclivity to fracture.¹⁰ A similar study by Nahum used a 2.9 cm diameter impactor and showed force values of about 4050 to 6300 N for frontal impact and 3050 to 3980 N for side impact.⁴¹ In another similar study by Allsop, the impacting areas consisted of a flat plate or a 6.45 cm² cylinder with velocities of 4.3 m/s and 2.7 m/s respectively. The mean fracture forces were 12390 and 5195 N respectively.³ Studies with access to such devices are uncommon however. In one such study, the experimenters tried to determine the forces in a car accident by purchasing dash panels from junkyards that had indentations in them from the passenger's heads impacting with the dash. They then put a model head in a "catapult" and adjusted the force values until they got the same dent parameters in new dash panels. As a follow-up, they examined the fracture tolerance of various bones using a 6.45 cm² impactor placed on the catapult arm. Fracture values of 120 and 180 g's were found for

the frontal bone, and they noted that increasing the area of impact increased the fracture point beyond the force generation capabilities of their device.⁵⁵

Similar to a free-fall impactor scenario, head drop experiments such as the ones carried out by Hodgson swap velocity vectors such that it is the impacting surface that is stationary and the body that moves. Impacts by this means were carried by multiple drops for each head, ranging from about 0.1 to 1.1 meters onto probes mounted on a load cell. The experimenters used profiles of various shapes including plates, 6.45 cm² cylinders, and hemispherical anvils. The actual area of impact was not measured in these experiments although the head was restrained by a cord to maintain the proper striking location during fall. Additionally, because fracture does not always occur directly at the impact site, it was not possible to give exact geometric coordinates for the impact. Forces ranged from 3114 to 7340 N of force in fracture scenarios.²³⁻²⁵

Other studies used a pneumatic striker instead of a free fall scenario. While this allows for precise velocity control and measurement of force, it does not match the sequence of events in an accident, where ballistic laws are in effect. In several studies lead by Yoganandan, measurement of force values was conducted at quasistatic (2.5 mm/s) and dynamic loading (7.1 to 8.0 m/s) with a 9.6 diameter hemispherical impactor. Since the actual area of impact was not measured in the study, the actual area of impact cannot be said with certainty, however force values for the frontal bone ranging between 4642 and 13600 N. Likewise values for the temporo-parietal bones range from 5603 to 612 newtons.^{60, 61}

2.2. Animal Testing

More commonly performed for injury predictions is cadaver testing. Using cadavers, it is possible to find the biomechanical properties of human tissue. Limitations to this technique include being unable to gain an evaluation of an injury based on behavioral changes stemming from damage to the brain and the small supply of cadavers available for medical testing coupled with the vast differences between biomechanical values between individuals.⁶⁰

In order to get a concept of soft tissue failures, animal models are generally used. Depending on the purpose of the experiment, several animal models of either in vivo or in vitro nature have been used. While some values received from animal models transfer directly to human thresholds for injury, other values must be translated by some factor given the different biomechanics of the animal model from the human system. For concussion, this difference can be shown by a 83% reduction in the angular acceleration needed to produce a concussion with 99% certainty when compared with the same acceleration for a rhesus monkey.⁴⁶ Using a hamster model, the optic nerve was stretched by gently manipulating a lasso to behind the eyeball and applying a force in order to demonstrate injury thresholds for axonal damage. The average strain required to produce mechanical injury was found to be $0.21 \text{ m}^2/\text{s}^2$, and the average strain to produce electrophysiological impairment was $0.18 \text{ m}^2/\text{s}^2$.⁶ Porcine models were also used to study DAI creation, and miniature swine were subjected to a 110° rotation about the coronal plane with peak accelerations of $(0.6-1.7) \times 10^5 \text{ rad/s}^2$. Widespread, multifocal axonal injury was found, most prominently about gyral roots and at the interface between gray and white matter.⁵²

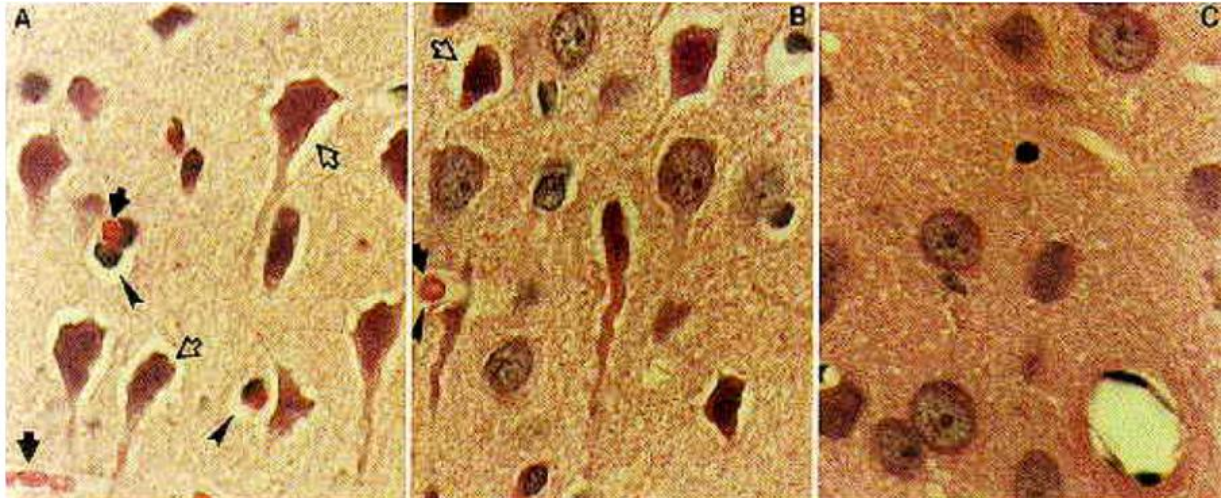


Figure 1: Damaged rat axons due to head impact. Neurons on the left show extensive damage denoted by arrows with shrinkage and disrupted blood vessels. Middle shows areas more distant from the impact, where less damage can be seen. The image on the right shows tissue distant from the impact.¹⁵

Rodent models are also common. In one study, a 450 gram weight was dropped upon a metal plate fixed to the skull, in order to prevent skull fracture. Two injury levels were created by allowing free fall of the weight from 1 and 2 meters in height. Histological examination of figure 1 showed no mortality was seen in the first group, while 59% mortality was seen in the 2 meter drop height cohort.¹⁵ A ferret model was used to with a pneumatic striker on the vertex of the skull. Contact velocities of $2.0 \text{ m}\cdot\text{s}^{-1}$ to $4.0 \text{ m}\cdot\text{s}^{-1}$ were simulated, with deformations of 2.0 to 5.0 mm. It was found that there were virtually no injuries seen in the lower velocity group, and near 100% fatality in the higher speed group.³³ Another rat model was created which used the metric of stress*time for the injury prediction chance.³²

When possible primate models provide a similar brain to that of humans. In an experiment regarding rotational effects along the sagittal and coronal planes on axon damage alone, with a 6-8 millisecond accelerative pulse, peak angular deceleration of 1-2

$\times 10^5 \text{ rad}\cdot\text{s}^{-2}$ and peak angular velocity of $475\text{-}510 \text{ rad}\cdot\text{s}^{-1}$, no significant difference was found in the histological examinations of the axons.¹⁸

2.3. Finite Element Modeling

One of the more useful models for studies of brain damage is that of the finite element simulation. In this model, computer software is used to approximate the material properties of an object and examine the interaction of that object as forces are applied. This is a highly valuable resource in cases where real world experimentation is tightly regulated, expensive, or impossible as is the case with human experimentation of injury thresholds. Core to the construction of a model are the values used to make it work. The more detailed the model is to be, the more components need to be modeled and the more accurate the properties of the material need to be. Since finite element models are approximations, they will not show the full truth of an occurrence, but they can be very helpful in approximating a result. In a finite model creation designed to study blast related neurotrauma, where a large amount of parameters were varied within the model, it was concluded that least relevant source of error is the assumption of linear kinematics. Much more significant to the results, and obtaining an accurate value for a simulation, were the material properties assigned to the model and the discretization error.^{50, 65}

Another error source lies in the fact that a model cannot tell the user if there is a value at an element that would correspond to an injury. Rather, the user must set a threshold for injury or compute the probability of injury occurrence for a particular value. In order to consolidate these down to a single measurement, a finite element model was formed for one study, in which accidents involving the head were reconstructed. The

conditions surrounding the accidents were fed into the model used, which had different material properties for white matter, gray matter, and the brainstem, as well as short and long time duration shear moduli. It was concluded that the strain of the brain multiplied by the strain-rate was the best

indicator of head injury, with the fit created by this plotted in figure 2 and $0.37 \text{ m/m} \cdot \text{d(m/m)/dt}$ yielding the 50% injury chance value.⁶³ This value is related to the stress*time metric used in the rat model created by Lamy.

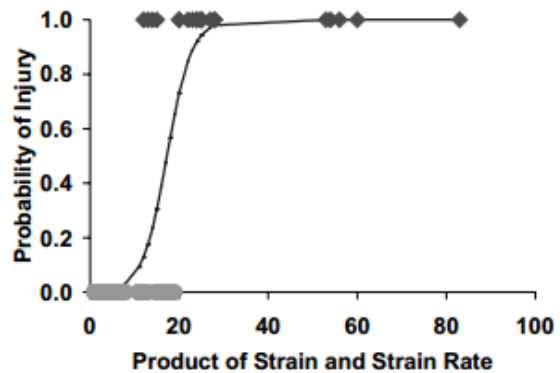


Figure 2: injury chance over $e \cdot de/dt$ as found from reconstructed data.⁶³

In order to simulate and achieve a similar risk function for subdural hematomas, a model of the brain was created with multiple bridging veins. The model used a Mooney-Rivlin hyperelastic law for the central nervous tissues, a shear modulus of 1.5 kPa, and a sliding contact surface for the cerebrospinal fluid. The model simulated frontal, occipital, and lateral impacts, and found that the bridging veins were most strained with, and consequently most inclined to fail, during impacts on the occipital region. It was found that a frontal impact with an HIC score of 362.6 yielded a bridging vein strain of 1.6%, and an occipital impact gave a strain of 9.5%. Lateral impacts showed zero strain to the bridging veins.³⁰ A mathematical model of the hematoma formation was found in a different experiment for bridging vein disruption. This model relates maximum allowable peak angular acceleration with the change in angular velocity. Thresholds were $\Delta 70 \text{ rad} \cdot \text{s}^{-1}$ for short term injuries, and $4500 \text{ rad} \cdot \text{s}^{-2}$ for lengthier injuries, with a continuously

differentiable function connecting them in figure 3.³⁵ A similar system was used for determination of maximum allowable DAI. Thresholds were found to vary for different brain masses, but the maximum angular acceleration was $1.6 \times 10^4 \text{ rad} \cdot \text{s}^{-2}$, and the maximum allowable change in angular velocity was $46.5 \text{ rad} \cdot \text{s}^{-1}$.³⁷

To study the effects of an impact to the skull, a force can be applied to a specific location on the skull. This was done in one model which utilized a mesh made from a CT

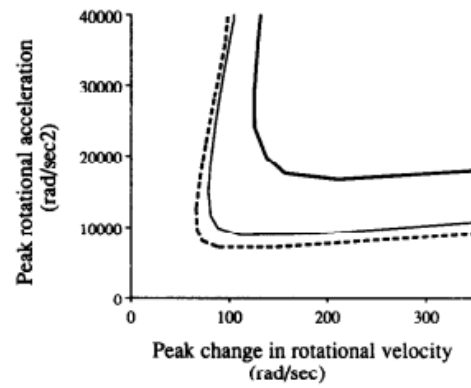
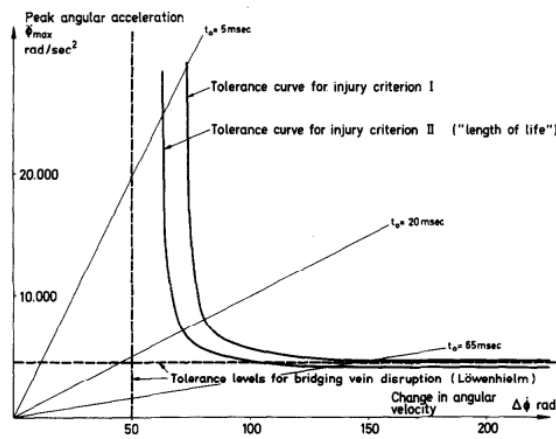


Fig. 6. DAI thresholds for a range of human brain masses. DAI tolerances for infant (500 g brain mass, heavy solid line) and adult (1067 g, solid line; 1400 g, dashed line).

Figure 3: Tolerance curves for hematoma arising from the bridging veins (left), and for DAI (right). Values that fall above and to the right of the threshold lines indicate a non-zero probability of injury development.^{35, 37}

image of a human skull and brain. A 16 kN force was applied to the front of the skull, as well as laterally in another simulation with a boundary condition of zero displacement set at the foramen magnum. Pressure waves within the skull for the frontal and lateral impacts were recorded. The frontal impact was found to generate a maximum pressure in the brain of 249 kPa. Lateral impacts were found to have a 6.67% greater pressure development on the coup side and a 14% higher tensile stress on the countre-coup side when compared to the frontal impact.⁴⁹ A similar model was created using additional layers of soft tissue such as skin and measured pressure data for impacts. The model

concluded that the additional layers of soft tissue were not as critical as the properties of the skull and brain.⁵⁷ An additional impactor finite element model predicted that the peak positive and negative pressures for a frontal impact occurred at the same time. Due to differences in wave formation in the skull, impacts to the occipital area had a peak negative pressure 3 milliseconds after the peak positive pressure.⁶⁴ Another multidimensional model used various linear impacts in the SIMon model. This model has some predictive capabilities for skull fracture, but requires finite element simulations to make them. Additionally, it uses a large mesh size, which can introduce errors into a finite element simulation. A linear impact of 98 g's, peak angular acceleration of 3951 rad/s² and peak angular velocity of 15.26 rad/s yielded a maximum principle stress of 71 kPa.⁵⁶ Also in the category of impact related neurotrauma is a simulation of a fall where the head struck at velocities of 1.5 and 6 m/s a simulated wooden floor with a thickness of 10 mm, density of 0.9 kg/m³, Young's modulus of 11 GPa, and a Poisson's ratio of 0.49. The 1.5 m/s simulation produced a maximum pressure of 53 kPa and a Von Mises stress of 12 kPa. The 6 m/s simulation produced a maximum pressure of 574 kPa and a Von Mises stress of 66 kPa with bone fracture.⁵¹

In a study of blast injury, a Hybrid III Anthropomorphic Test Device model was modified to include a head mesh from the VOLPE National Research Transportation Center. The model was faced with a 550 kPa overpressure wave to the front of the simulated head. The maximum recorded Von Mises strain in the anterior corpus callosum was 0.0125 and the corresponding strain in the posterior corpus callosum was 0.0095.²² Additional Von Mises stress values can be seen in figure 4, which shows the rippling effect in tissue over time that is seen in impact. Another blast simulation utilized a plane-

strain model of the human head and brain, positioned within a blast domain model using the LS-Dyna hydrocode. The study looked at the effects of a cavitation model and a noncavitation model, and found small differences between the two when exposed to large blast overpressure waves – namely that the cavitation model showed more damaging loads imposed upon the brain at higher pressure waves. The model also showed a higher prevalence for contre-coup over coup injury.⁴⁷

2.4. Predictive Models

In order to describe the result of an injury, scales must be constructed that allow both precise and accurate prediction of injury states. For head injury, this can be difficult as many experiments simply show a binary nature of healthy or injured tissue. In every experiment conducted, there is overlap where an injury for one subject resulted in no injury for another subject. Therefore, translation scales cannot show a binary jump at a threshold, but rather a probability curve of injury values given a set of impact conditions. Several scales make an attempt at this, but all have limitations. Summarized in table 1 are

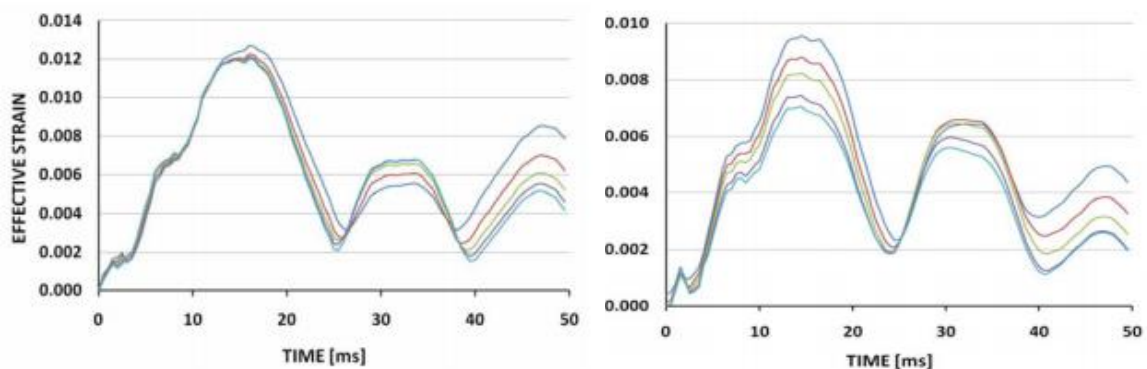


Figure 4: Strains on the corpus callosum. Strains on the anterior corpus callosum can be viewed on the left whereas strains upon the posterior corpus can be seen on the right.²²

the Gadd Severity Index (GSI), Head Injury Criteria (HIC), the Head Impact Power (HIP), the Simulated Injury Monitor (SIMon), the Louis Pasteur University Model (ULP), the Glasgow Coma Scale (GCS), the Abbreviated Injury Scale (AIS), and a quantized method of describing injury based on CT imaging. Of these, the HIC and HIP are pure equations that take into account accelerative forces on the center of mass of a subject but fail to adequately describe several conditions of brain injury and are of very little use for describing skull fracture. The SIMon and ULP are low resolution finite element models of the head which require acceleration inputs and a subsequent lengthy calculation time. Finally, the AIS and GCS are scales used in a hospital setting that allow classification of the severity of a head injury but not prediction capability. The Linear Skull Fracture Criterion shows promise as a predictive statistic, but fails to account for the complex details of a collision like location and impactor shape.

Injury Scale	Formula	Measures	Inputs	Limitations
Gadd Severity Index	$\int_{t_1}^{t_2} a(t) dt^{2.5}$	linear acceleration injury risk	linear acceleration	Same as HIC, but also discounts variable acceleration
Head Injury Criteria	$\left\{ \left(\frac{1}{t_2 - t_1} \int_{t_1}^{t_2} a(t) dt \right)^{2.5} (t_2 - t_1) \right\}_{\max}$	linear acceleration injury risk given a variable acceleration	linear acceleration	Used in crash testing. Uses acceleration from center of mass, does not take into account forces such as rotational acceleration, which is highly correlated to concussion.
Head Impact Power	$C_1 a_x \int a_x dt + C_2 a_y \int a_y dt + C_3 a_z \int a_z dt + C_4 \alpha_x \int \alpha_x dt + C_5 \alpha_y \int \alpha_y dt + C_6 \alpha_z \int \alpha_z dt$	linear and rotational injury risk	linear and rotational accelerations in Cartesian coordinates	Expansion of HIC. Little use for hematoma or fracture
Linear Skull Fracture Criterion	$\ln\left(\frac{P}{1-P}\right) = C_1 * \ln(strain) - C_2$	Skull fracture risk given SFC	g-force	Does not distinguish between any variables besides g-force
Simulated Injury Monitor	Finite Element model	Strain, dilation, and relative motion damage	acceleration field	Uses a rigid skull with low resolution. Low accuracy of results

Injury Scale	Formula	Measures	Inputs	Limitations
Louis Pasteur University Model (ULP)	Finite Element model	Von Mises and strain energy leading to SDH, strain leading to skull fracture	acceleration field	Low resolution FE model using acceleration fields. Decent predictive ability
Glasgow Coma Scale	qualitative numerical scale from 3 to 15	consciousness level	Eye, verbal, and motor reactions to stimuli	Used in hospital settings. Qualitative scale of patient responses that can result in low accuracy of results. Verbal response cannot be used in tracheated patients
Abbreviated Injury Scale	qualitative numerical scale from 1 to 6	Injury severity of multiple regions	severity score for all parts of the body	Used in hospital settings. Subjective measurement of injury based on evaluation. Not a predictive tool for injury.
CT classification	combination measurement of midline shift and lesion area	degree of abnormality in CT image	CT image measurements	Used in hospital settings. Provides good diagnosis, but expensive test. Not a predictive tool for injury development.

Table 1: Comparison of various quantification scales for head injury.

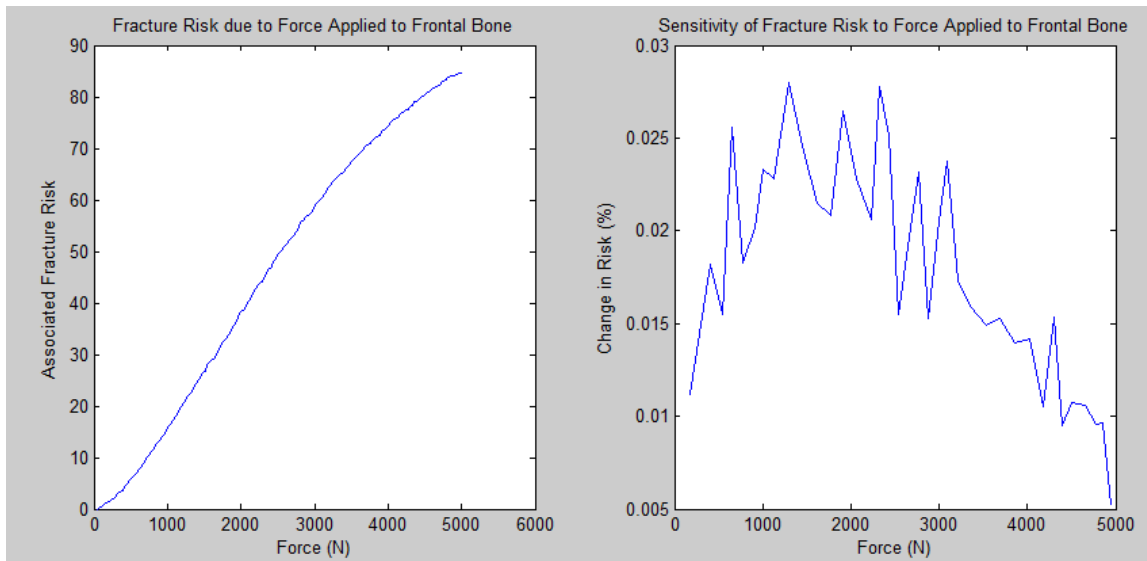


Figure 5: Fracture risk curve (left) and sensitivity analysis (right) originally developed by Cormier and expounded here.

All of the equations for determining injury score are mired in controversy.

Experts disagree over what thresholds represent a suitable tolerance limit as well as the maximum allowable pulse length for the HIC. Other papers conclude that the very foundations of the HIC formula are invalid, with other factors besides linear acceleration not directly leading to injury.⁴² Other studies have shown very little correlation between the HIC predictor of injury and in-hospital ratings such as the AIS.⁴⁵ Nevertheless, Cormier shows a risk function created from several real world head impacts, despite a large amount of assumptions. This function and its accompanying sensitivity plot can be viewed in figure 5.¹⁰ It is extremely difficult to create a reliable injury prediction model in this way as it is exceedingly difficult to fully capture the complexities of multiple deformable components with a single rigid body analysis. Compounding to this difficulty is the variability of physiology between ages and sexes, not to mention the variability within these groups. This variation forces equations like the HIC and the HIP to use a generalized model of the skull. Additionally, these formulae fail to distinguish between

mechanical and biological damage to tissue, which can be important as biological disruption in messaging between neurons can be disrupted long before mechanical failure occurs.

Of note, the added computing terms of the HIP when compared to the HIC suggest that it should be more accurate for injury, but this is not the case in all modes. The HIC showed a higher degree of accuracy based on reconstructed accidents of more traumatic injuries, where linear acceleration dominated and rotational acceleration was less important.³⁸ More accuracy was also seen in the prediction of SDH. This suggests that the HIP does not have proper scaling factors for the prediction of neurological injury, despite the additional terms when compared to the HIC. While these equations can be used to predict mild, moderate, or severe brain injury as well as SDH or fracture, the varying accuracy between them suggests that they can be improved to form a unifying equation that can be manipulated for risk factors of each injury archetype.

Chapter 3: Computational Sensitivity Analysis of Fracture Thresholds in Literature

Published results from papers in the literature review were sorted and presented in figure 6. Since studies rarely showed exact geometric coordinates for the areas of impact on the skull, examples of the fracture threshold force are shown based on the general classification of the frontal bone or the side (temporoparietal). These tolerance values were compiled and analyzed for trends, to attempt to derive a model. Correlation plots were conducted using the limited data available from publication. The simple multivariate

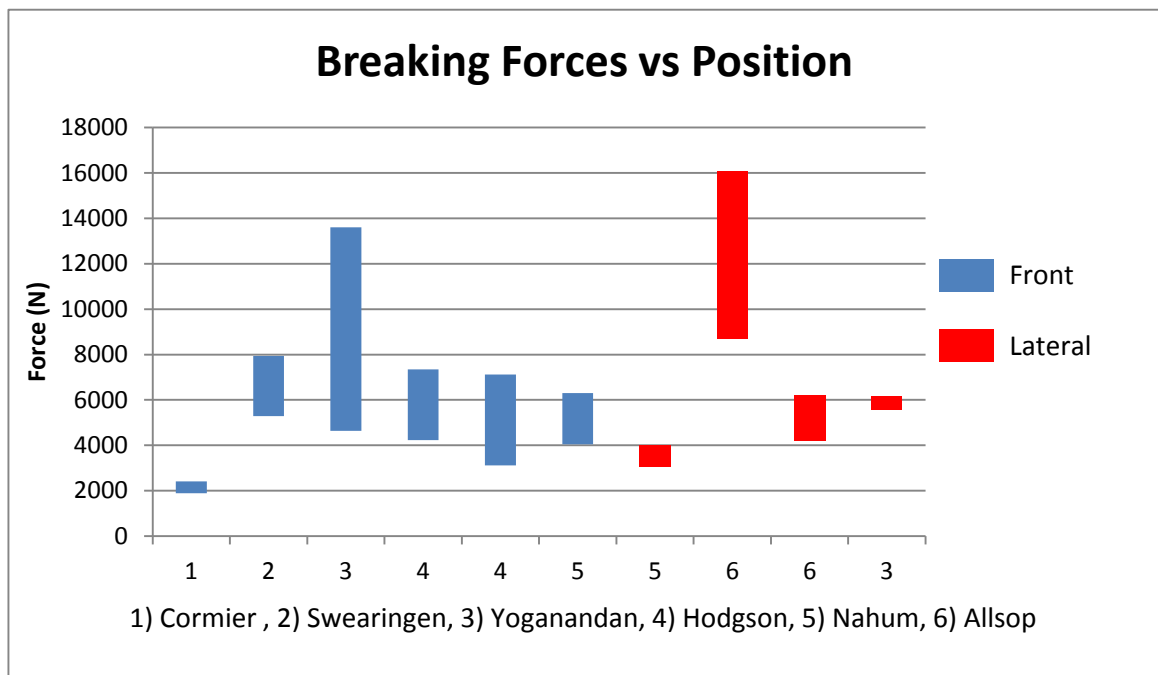


Figure 6: Chart of selected failure values sorted according to location and author.

equation shown in equation 1 was achieved with an R^2 of 0.412 where location was 1 for the frontal bone and 2 for the temporoparietal area. Area of impact was not able to be included in the equation due to insufficient data. This is due to the fact that most studies do not report the exact area of impact. Of those that do report the impactor area, the impactor was often a hemispherical anvil with a varying effective cross section depending on the deflection induced in the bone.

$$Force = 5534 + 417 * Weight - 369 * Velocity - 328 * Location \dots \dots (1)$$

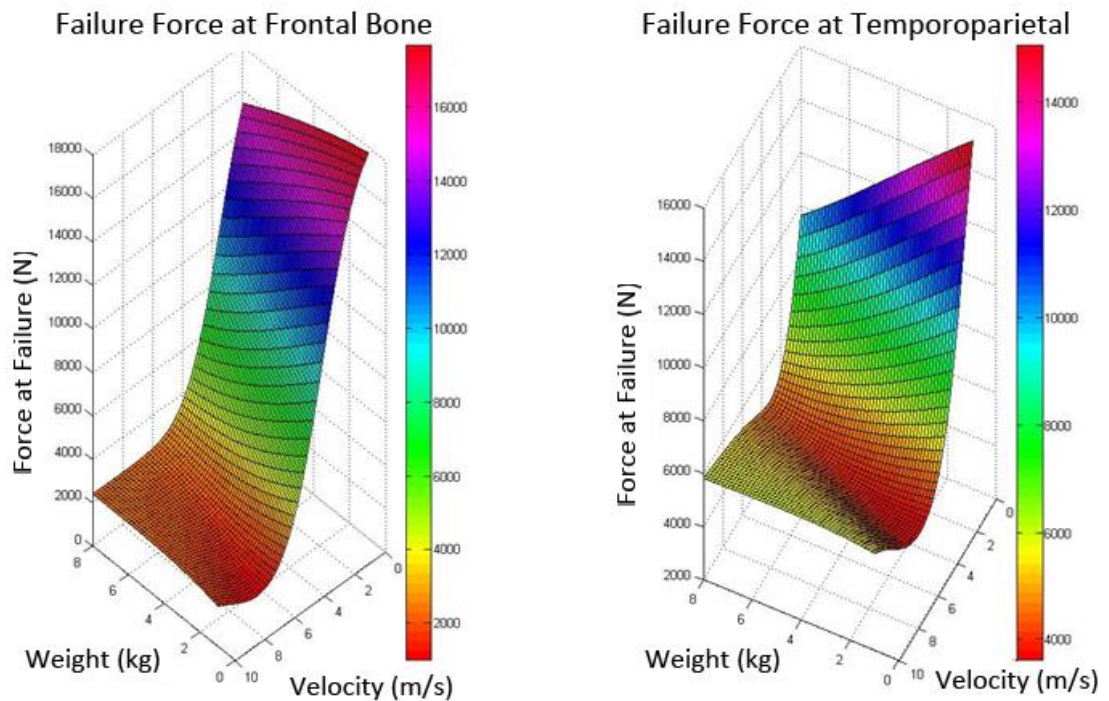


Figure 7: Neural Network profile of fracture force based on weight and velocity of impactor for front and lateral impacts.

The model was refined to an R^2 value of 0.978 using a neural model of the data, as seen in figure 7. The neural network was created via the holdback method, where 33.3% of the data was excluded from the model creation and used to verify against

overfitting the data by inclusion of noise. The equations used in the model can be seen below, in equation 2.

$$\begin{aligned}
 F &= 13562 + 1303 * H1 - 9703.7 * H2 - 3057 * H3 \\
 H1 &= TanH(0.5(-8.2 + 0.561 * Weight + 0.820 * Velocity + 0.554 \\
 &\quad * Location)) \\
 H2 &= TanH(0.5(-4.61 + 0.164 * Weight + 0.822 * Velocity + 1.894 \\
 &\quad * Location)) \\
 H3 &= TanH(0.5 \\
 &\quad * (7.20 + 0.022 * Weight - 0.0776 * Velocity - 3.516 \\
 &\quad * Location)) \dots \dots \dots (2)
 \end{aligned}$$

The sensitivity of this equation to the weight, velocity, and location was calculated and found in Figure 8. This model shows the greatest fit within the input parameters used. These are from 0.002 to 7.1 m/s and 1.1 to 12 kg. Location should be treated as an ordinal variable and is not continuous.

It is well known that failure conditions for materials, both biological and otherwise, depend on a number of factors including load rate. Most materials are able to accommodate a small load for a long duration. The safe duration for bearing a load drops off as the load increases. This presents with a high required fracture force given a speedy collision. Conversely, for a collision in which a force is slowly applied, a lower fracture force would be required. As the duration of the collision continues to increase however,

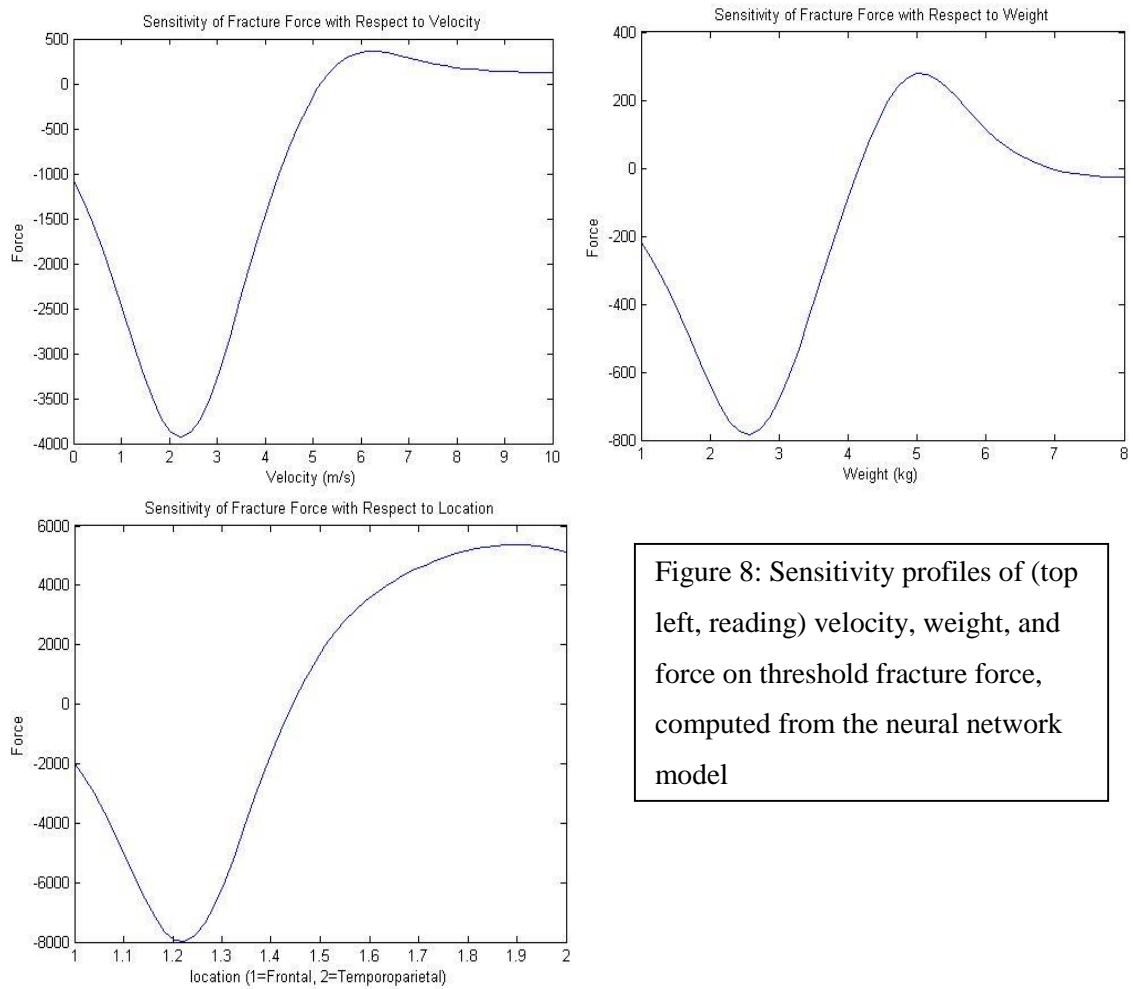


Figure 8: Sensitivity profiles of (top left, reading) velocity, weight, and force on threshold fracture force, computed from the neural network model

the force tolerance maintains a relatively constant level, due to the sudden impulse of force. This equation shows this decrease in force tolerance due to increasing impact durations, as seen in the negative derivatives in figure 8. As the velocity approaches quasistatic tests, the required force to fracture the skull decreases. An inflection point was found for the velocity at 4 m/s, which indicates that speeds lower than this is increasing quasistatic effects compared to dynamic testing.

Examination of the weight term reveals that increasing the weight decreased the force required to fracture the skull up to the 4.2 kg mark. After this point, the force required to fracture the skull increased. This could be brought about by the effects of

impact area upon the skull as the larger weights reported utilized a flat striking surface while smaller mass weights tended to have a more pointed surface.

Though it is known that side impacts have a higher risk for concussion and other forms of brain damage when compared to frontal collision, several studies have shown conflicting values for the risk functions of skull fracture. The equation here predicts that there is a greater sensitivity for fracture at low velocities for side impacts (~13050 N) compared to frontal impacts (~16050 N). At high velocities however, the situation is reversed, with frontal impacts becoming more sensitive (~2000 N) when compared to side impacts (~6000 N).

It is impractical to test all possible loading rates on cadavers given the continuum of velocities, loads, and positions. Nevertheless, researchers strive to make an accurate model of the human head given the resources available. This model was validated against the binary data from controlled studies, and the mathematical models produced herein can be used to glean information from the areas between the validated points. This equation promises to help fill the gaps in our knowledge by analyzing the data currently available. Exact location on the skull and the exact area of the contacting surface with the skull rather than the approximate area based upon the geometry of the impactor were the two most commonly omitted data points. Based on this finding, future analysis of skull fracture thresholds using human or animal models should be sure to make note of all input parameters. Both of these statistics could also benefit from better representation in the literature by means of future studies.

Chapter 4: Computational Materials and Methods

4.1. Source Image CT Details

The model used herein was developed using a CT scan from a willingly donated cadaveric head of an adult male who had died of unrelated causes. The CT scan used a slice thickness of 0.95 mm in each orthogonal direction. Maximum dimensions of the skull were 156.3 mm in the transverse plane, 186.3 mm from brow to the external occipital protuberance, and 143.0 mm from the vertex to the foramen magnum. Average skull thicknesses at the frontal bone were 7.82 mm, 7.80 mm for the occipital bone, 6.21 at the vertex, and 6.42 mm for the temporoparietal bone. These values can be seen in figure 9. Average bone density was 842 Hounsfield units (HU) measured across both the cortical and cancellous bone and had a standard deviation of 255 HU. These values render the skull into the 50% category for males.

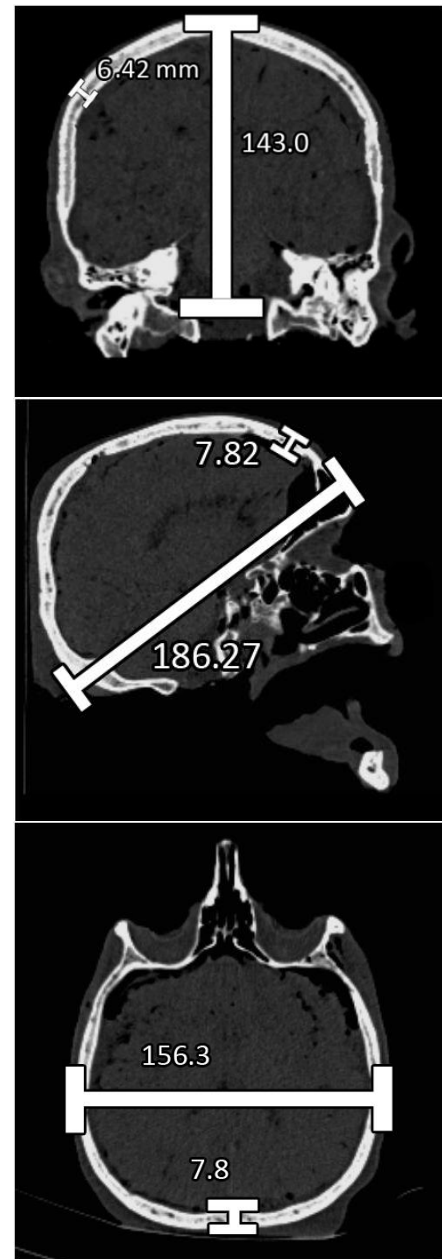
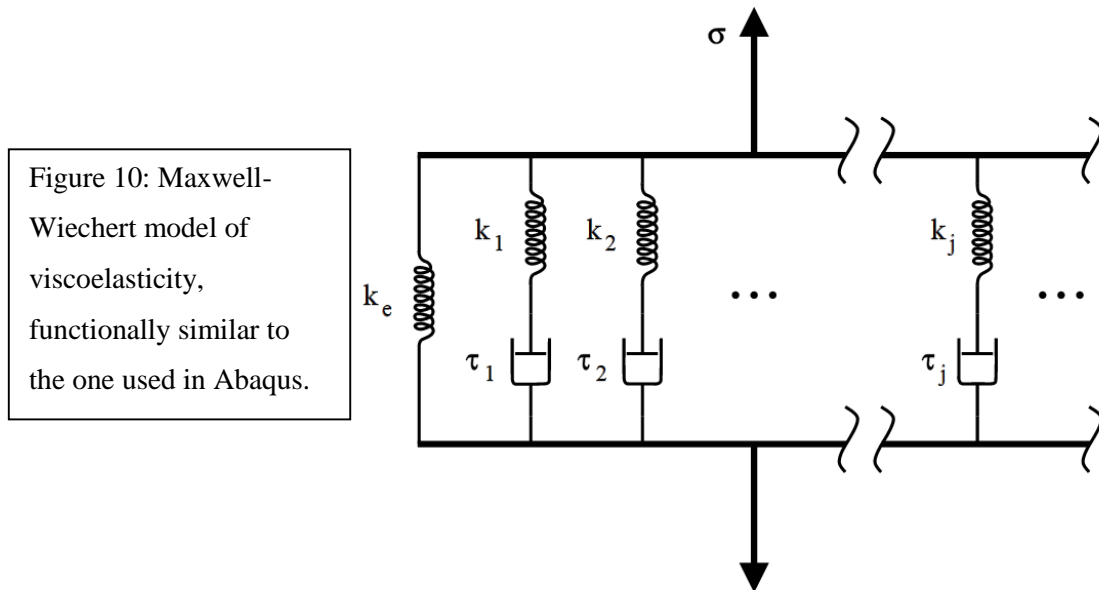


Figure 9: CT images of the (top to bottom) coronal, sagittal, and transverse views of the skull used to create the model.

4.2. Meshing

Bone was thresholded from the model using Mimics software with a high pass value of 226 Hounsfield units and spot checked in each slice for accuracy in order to capture trabecular bone and fine boney sections in the sinuses.⁴³ The solid body model created from this used a maximum element length of 4 mm to form a mesh of elements. The model contained 209,188 nodes and 969,575 tetrahedral element topology 4 elements (TET4). TET4 elements combine 4 non-planar nodes into a 4-sided tetrahedron with 6 edges and 4 faces. Each of the nodes in the element are connected by linear polynomial shape functions specified using the local coordinate field of the element. These elements are the simplest arrangement of nodes and will sacrifice some accuracy in favour of speed when used at low mesh densities. It was then exported into Abaqus for finite element analysis where it was converted into Continuum 3-D, 4 node element types (C3D4), which are also tetrahedral in shape. These elements have three integration points



for each direction, for a total of 27 integration points per element. The high density used in this model improved upon the accuracy and made them sufficient for calculations while maintaining the speed of calculations to under 16 hours per simulation. This is in comparison to other common use head models, such as a model developed in 1980 by Hosey and Liu that has 637 elements.²⁸ More modern models include the SIMon, which has 19,417 elements and 17,651 nodes and the ULP model, which contains 10,500 elements and 12,000 nodes.^{56, 59} Not all of these elements are included in analysis for the skull however; in both of these, elements are allocated for tissues other than the skull.

4.3. Viscoelastic Modeling

The skull was modeled as a viscoelastic body with a piston and dashpot system similar to that seen in figure 10, in order to capture the full effects of the impact upon the skull. Many studies, such as the SIMon and the ULP, have approximated the skull or other bones as purely elastic bodies. In these studies, the authors are generally interested in the force transfer from the initial force generation event, through the bone, and into other tissue. As such, many studies involving the brain use this approximation on the skull, which can yield inaccurate data for stress distributions in the skull. It is well known in literature that wet bone, as experienced in vivo, contains a viscoelastic element. Inclusion of these terms into the model here sought to improve the overall accuracy of the model. In order to do this, Prony series terms for viscoelasticity were used. G_i was 0.1346 Pa and τ_i was 117.85 s.¹³ Prony series analysis utilizes a minimization algorithm that corrects for errors between the predicted and measured values to represent the viscoelastic nature of the data. It then decomposes the data in a manner similar to that of a Fourier transform.

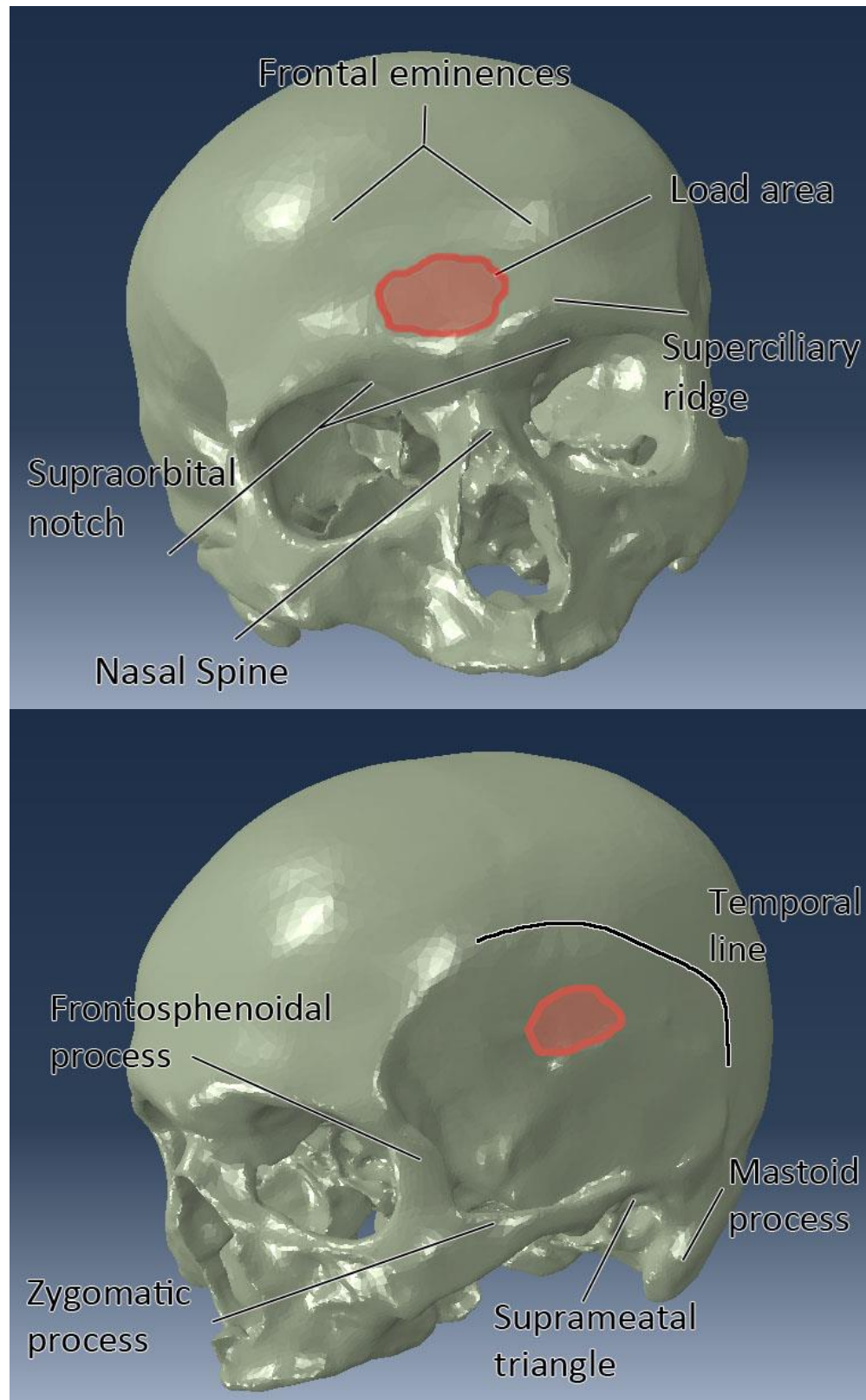


Figure 11: Force location with respect to anatomical landmarks on the skull for (top) front and (bottom) lateral modalities.

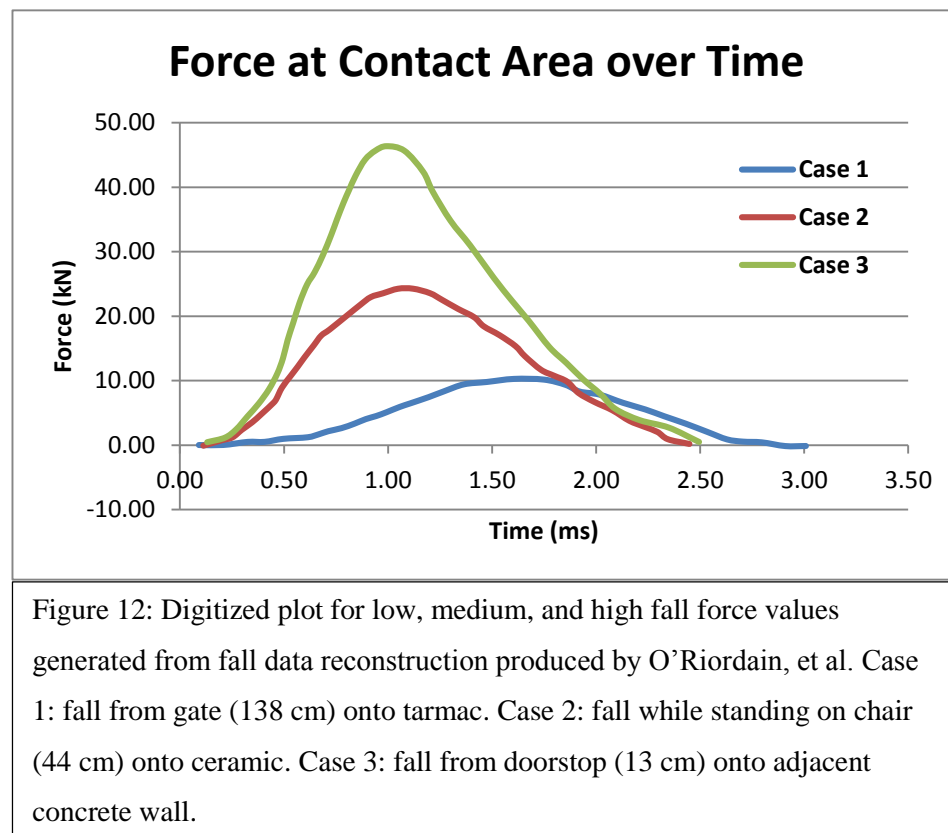
In addition to viscoelastic constants, a Young's modulus of 18 GPa, density of 2000 kg/m³ and a Poisson's ratio of 0.3 were used, as per common literature values for the skull. These values were considered to be isotropic. Though the skull has anisotropic components to it, most of the skull is composed of cortical tissue, which has less of an anisotropic element to it than trabecular bone. In addition, another anisotropic element in the skull, cranial sutures, were not modeled. Sutures naturally provide a very small degree of flexion to the skull, but ossify over time. Because of this, the assumption of isotropic bone does not cause a high degree of error in the model.

4.4. Force Modeling

Forces were uniformly distributed over a 300 mm² area in the “hat brim” region for the frontal and lateral locations to mimic the area impacted in falls as this is the most common region of the skull to be impacted in a fall. The area that the impact covers in a typical fall depends upon the object struck. A sharper, more pronounced, or stiffer object would tend to present with a smaller impact area. The frequency with which different objects are struck was not available in literature at the time, so typical areas of impact in a fall are not agreed upon. The value of 300 mm² was chosen as a value that would be comparable to the size of the hat brim area. The lateral force distribution was centered 53.9 mm over the suprameatal triangle and 57.5 mm dorsal to the frontosphenoidal process. It consisted of a roughly elliptical shape following the contours of the element borders of the skull with a semi-major radius of 12.1 mm and a semi-minor radius of 7.65 mm. The frontal force profile was centered over and located 40.7 mm above the nasal spine and was likewise an ellipsoid following the contours of the elements on the skull.

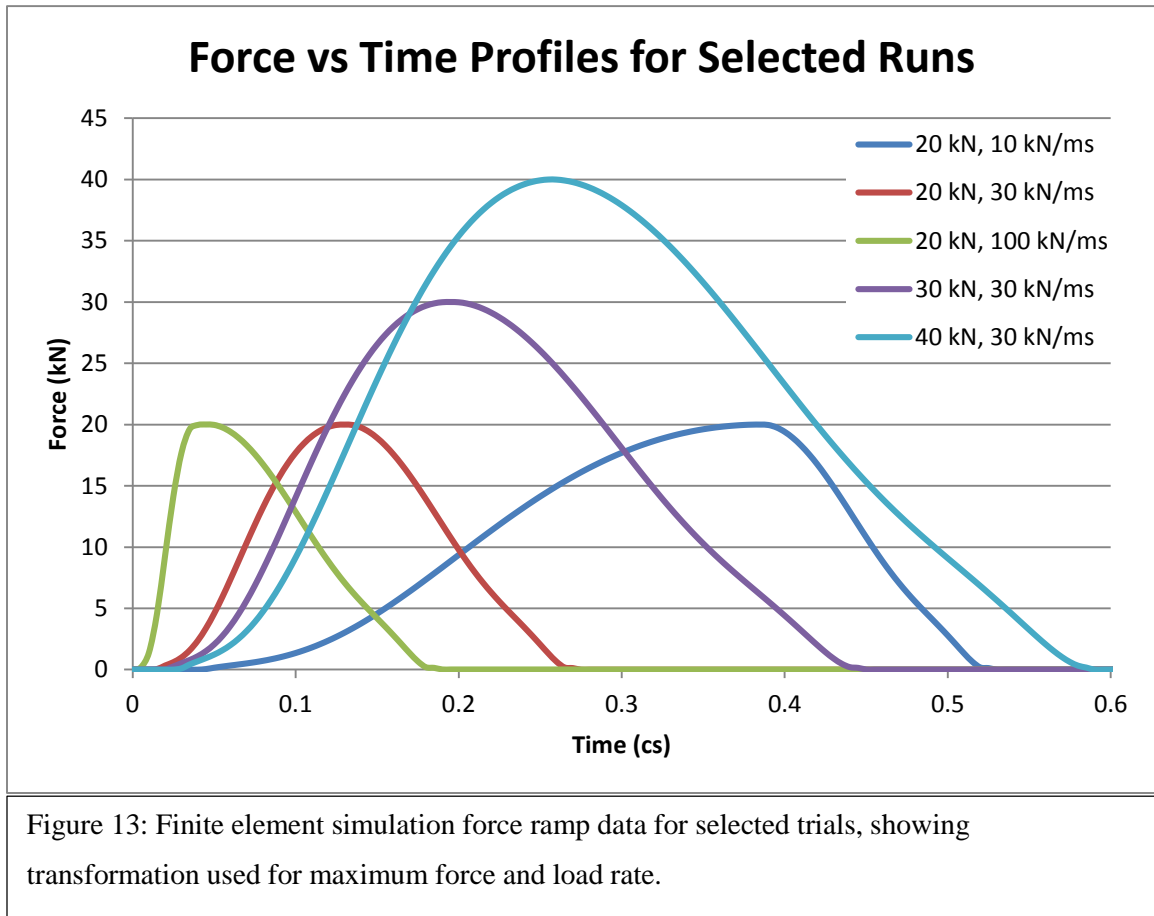
The semi-major radius was 12.28 mm and the semi-minor radius was 7.98 mm. These locations and approximate force areas can be seen in figure 11.

The magnitude used for the force was also designed to mimic the forces experienced in a fall. Fall data was reconstructed by O’Riordain and several force versus time plots were created based on the differing situations. Maximum forces for each simulation were found to range from 10 to 50 kN and maximum load rates between 10 to 100 kN/ms. Forces in the simulation were assumed to be directed normal to the skull, pointing towards the interior. Figure 12 shows examples of force curves from falls with various energies. Of these examples, only case 1 and 2 resulted in fracture of the skull based on the analysis by O’Riordain. These plots were digitized in order to generate an equation for force as a function of time. The medium force value (case 2) was used here and fit to the 9th degree polynomial seen in equation 3 from $t=0$ to $t=2.5$ with an R^2 of



0.998. This has a maximum force of 24,028 N and a maximum load rate of 43,878 N/ms. In order to adjust the force curve to better match the digitized data, the negative values at $t=0$ and the values after the local minimum at $t=2.42$ were both set to zero. This improved the R^2 value to 0.999. Force data was then generated for each run by scaling this equation to match the maximum force and load rates.

$$Force = 12368t^9 - 145961t^8 + 734204t^7 - 2049679t^6 + 3448499t^5 - 3517100t^4 + 2036925t^3 - 572817t^2 + 8181788t - 4424 \dots \dots \dots (3)$$



Based on examination of the fall data, to capture the range of fall impacts, 5 maximum force values of 10, 20, 30, 40, and 50 kN were used by scaling the output of the equation. Load rate values of 10, 15, 30, 50, and 100 kN/ms were used based on the proclivity for lower load rates seen in the literature. This was achieved by scaling the input time variable. The offloading rate was kept constant across each of these trials using the curve profile found by O’Riordain such that only the load rate and the maximum load varied. An additional test utilizing a load rate of 70 kN/ms was implemented for the all loads as a large jump was seen in the value of the resultant forces between 50 and 100 kN/ms. Representative curves showing the transformation used can be seen in figure 13.

4.5. Boundary Conditions

Boundary conditions for the frontal tests affixed the skull about the coronal plane, and lateral tests affixed about the sagittal plane. Initially, efforts were made to create boundary points about the foramen magnum; to mimic attachment points for the skull. This created an artifact in the stress distribution such that dispersal happened at the boundary conditions instead of at the impact site. Therefore, the current conditions were used to immobilize the head. Examination of the results showed that this regime eliminates artifacts from the boundary conditions as there was not a significant concentration of stress at the boundary conditions when compared to the stress at the impact site, which is shown in figure 14.

A simulation time of 10 milliseconds was used, which allowed for each test to achieve its peak von Mises stress value. For the 100 kN maximum load tests of 10 and 15

kN/ms, this resulted in truncation of the force offloading curve. Analysis of the forces generated however revealed that this did not have an effect on either the loading of the elements or the maximum load achieved. Simulations were run with an initial increment size of 10 nanoseconds and a maximum step size 50 nanoseconds using implicit analysis. Each simulation was run on an Intel i7 processor with 8 GB of RAM and averaged 14 hours of simulation time before completion. Results from each simulation were then imported into JMP for analysis. These results were found to converge using strain energy to within 0.5% by decreasing the seed size.

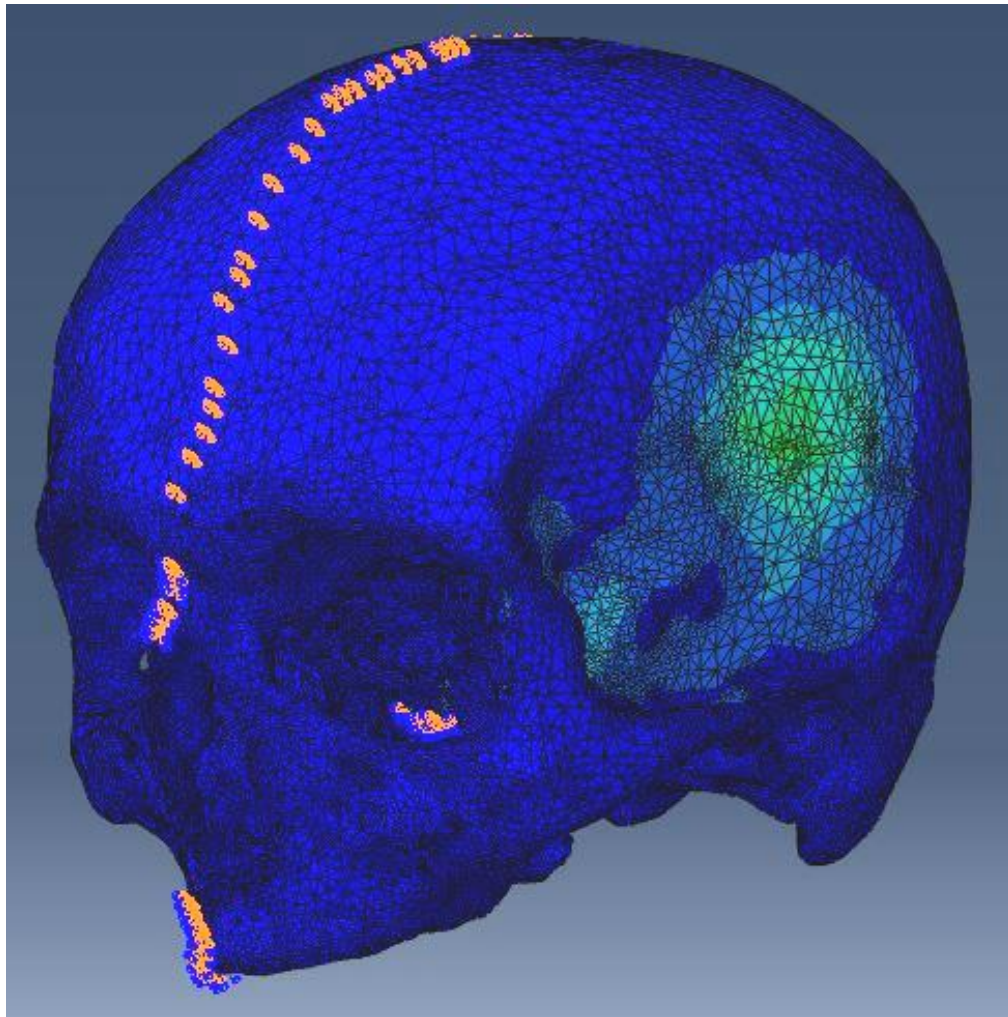
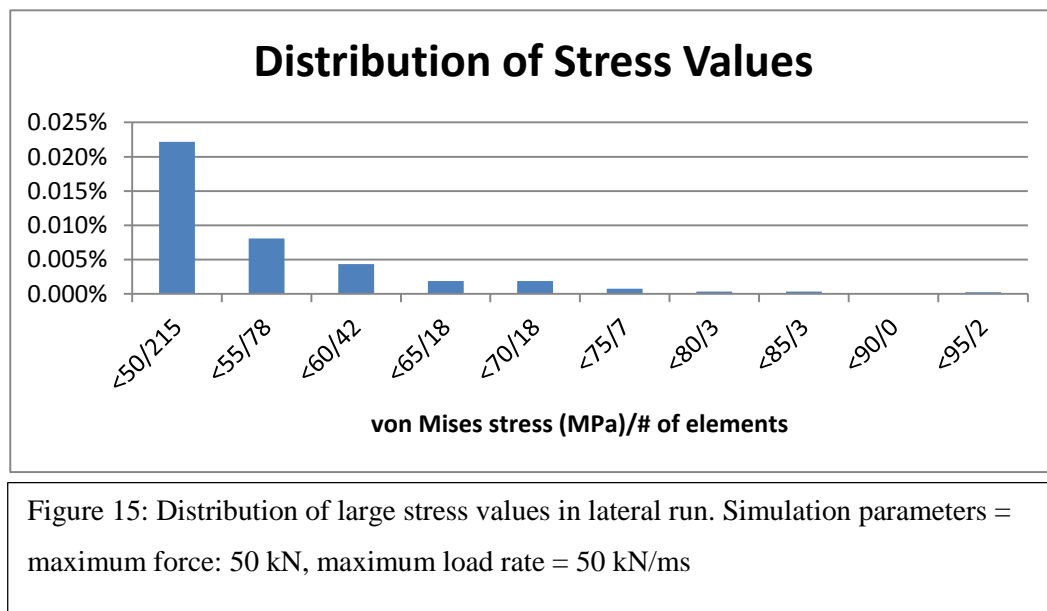


Figure 14: Boundary conditions for lateral loading test and force application. Simulation parameters – maximum load = 40 kN, maximum load rate = 50 kN/ms

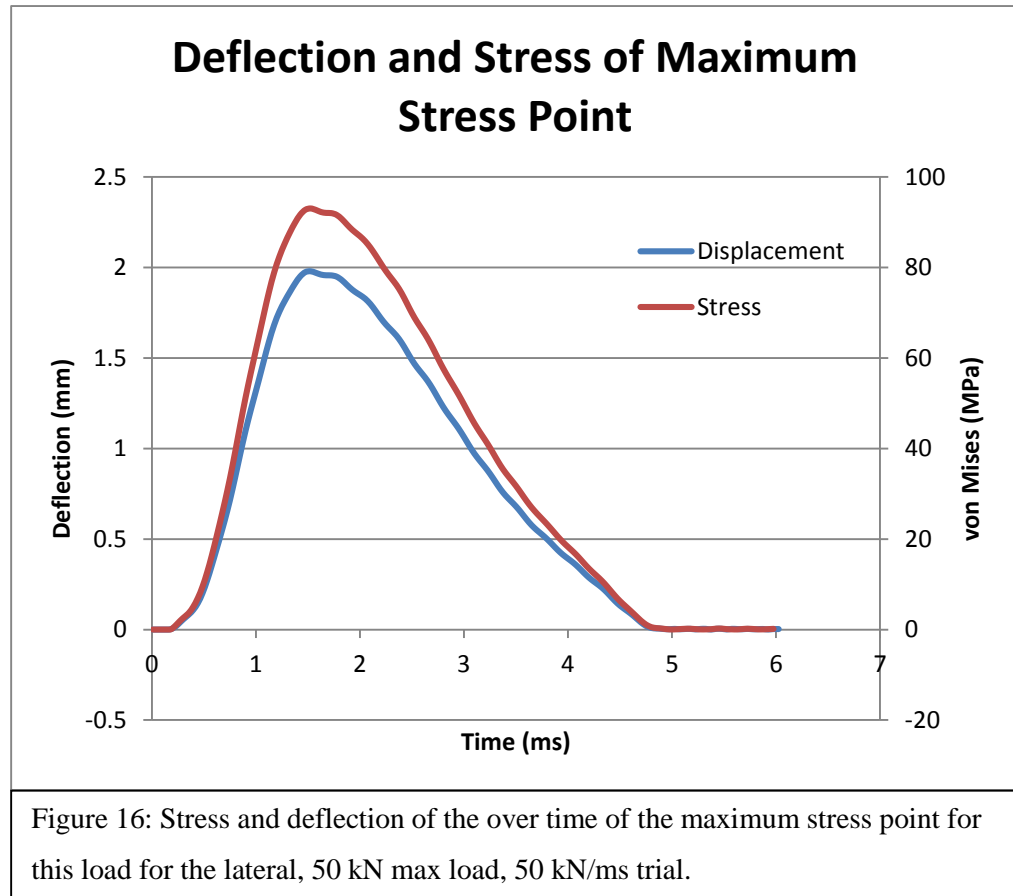
Chapter 5: Results of Finite Element Analysis

This chapter presents the results obtained from the analysis of the current study. Both von Mises stresses and deflection were recorded for each simulation. Details for these statistics, including maximum values, location of said values, distribution of such values over time have been recorded and are shown here.

Statistical analysis of results was carried out using JMP statistical software. To avoid isolated outlier points due to artifacts of the discretized finite element process, the 99.993rd percentile data point was used for each analysis. Repeated runs of the same initial conditions showed that there was no significant difference between multiple runs for this point while there was some evidence to reject uniformity in the prior points for each run ($P=0.18$).



Once results were obtained, they were fit using a linear combination least squares analysis and also with a neural network model. Neural networks are able to fit data very accurately, but can overfit noise in the input data. They are also less accurate for extrapolation of data outside of its input range.



5.1. Von Mises Stresses

Von Mises values ranged from 13.95 MPa to 94.97 MPa depending on the input parameters of the simulation, with higher load rates and maximum loads developing a larger von Mises stress. A typical distribution of stress values for each element can be

seen in figure 15, which shows a histogram of the results of a lateral simulation with a maximum applied force of 50 kN and a maximum load rate of 50 kN/ms. Figure 16 shows the loading and deflection of this element in a stress over time diagram of the same simulation. In the frontal and lateral cases, the majority of stress distribution was seen at the contact site of the force, with some areas of high magnitude extending from the site. Most noticeably, some force was seen in the sinuses, with a concentration in the sphenoid. This concentration of force in the impact site and sphenoid can be seen in figure 14, while figure 17 highlights the location of the maximum force of each run. The compendium of all stress results can be seen in table 2.

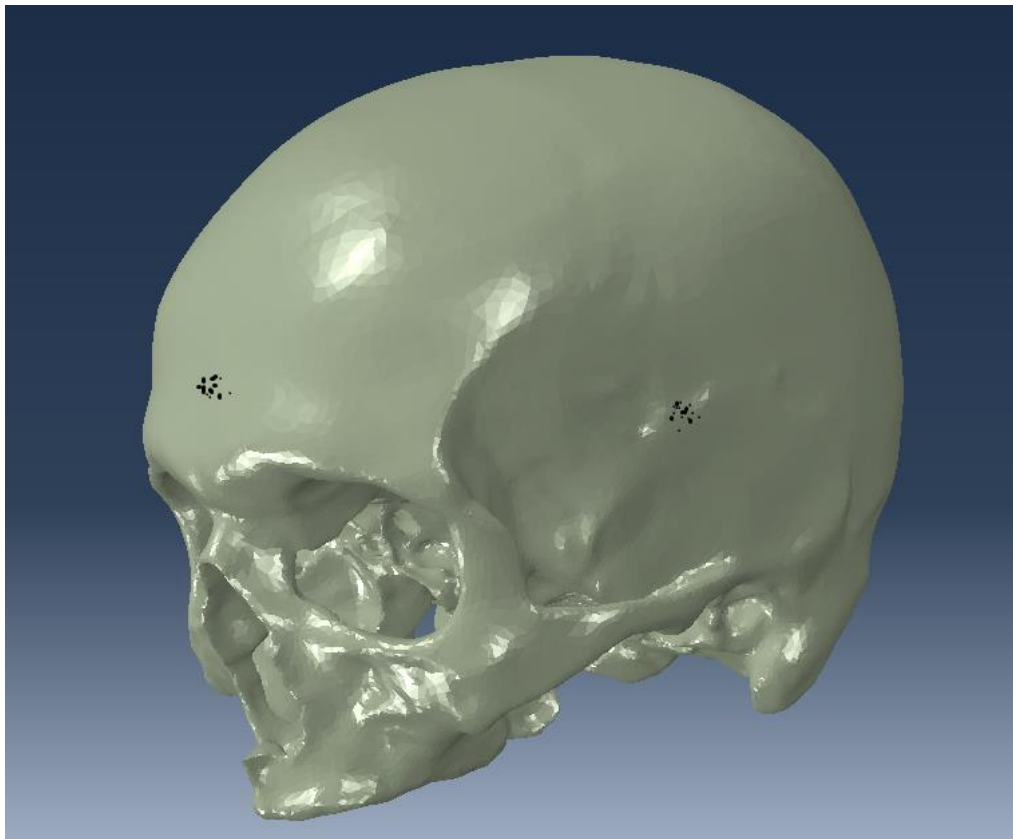


Figure 17: Distribution of maximum stress values across all tests. Each maximum value is included as a point. Concentration of points indicates a concentration of maximum forces.

		Lateral (max stress)					
		Load Rate (kN/ms)					
		10	15	30	50	70	100
Max Load (kN)	10	16.05	16.11	16.37	18.19	21.66	26.76
	20	33.00	32.99	33.02	33.38	35.19	37.86
	30	51.66	51.65	51.66	51.90	52.07	52.31
	40	72.03	72.03	72.08	72.33	72.62	73.04
	50	94.42	94.46	94.51	94.58	94.74	94.97

		Frontal (max stress)					
		Load Rate (kN/ms)					
		10	15	30	50	70	100
Max Load (kN)	10	13.95	13.98	14.19	15.76	18.75	23.15
	20	28.53	28.52	28.54	28.84	30.40	32.70
	30	46.10	46.08	46.06	46.25	46.39	46.59
	40	64.21	64.19	64.22	64.41	64.66	65.02
	50	82.24	82.26	82.28	82.33	82.45	82.63

Table 2: Maximum stress values for each simulation.

5.2. Deflection Values

The forces exerted on the skull also cause deflection into the cranial cavity. These forces can put pressure on the brain, transmitting the forces to the soft tissue. Maximum deflection values ranged from 0.42 mm to 2.37 mm depending on input parameters. Deflection magnitudes can be seen in figure 18 which shows the 50 kN, 50kN/ms test. As shown previously, figure 16 shows the deflection over time of this element. A table of the maximum results can be seen in table 3.

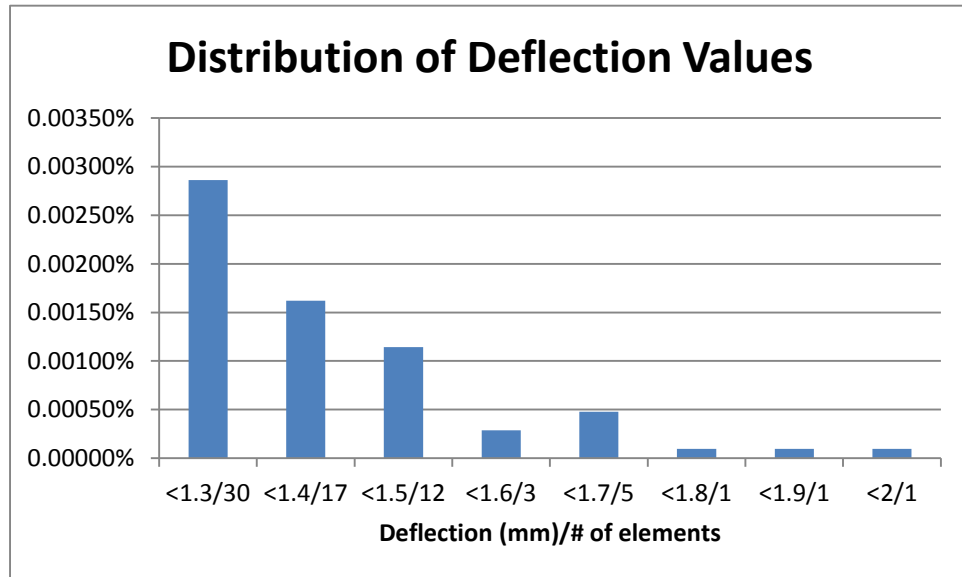


Figure 18: Distribution of large deflection values in lateral run. Simulation parameters = maximum force: 50 kN, maximum load rate = 50 kN/ms

		Lateral (displacement)					
		Load Rate (kN/ms)					
		10	15	30	50	70	100
Max Load (kN)	10	0.335	0.336	0.341	0.379	0.452	0.558
	20	0.688	0.688	0.689	0.696	0.734	0.789
	30	1.078	1.078	1.078	1.082	1.085	1.090
	40	1.502	1.502	1.504	1.508	1.515	1.524
	50	1.968	1.968	1.972	1.972	1.975	1.983

		Frontal (displacement)					
		Load Rate (kN/ms)					
		10	15	30	50	70	100
Max Load (kN)	10	0.292	0.292	0.297	0.330	0.392	0.484
	20	0.597	0.597	0.597	0.603	0.636	0.684
	30	0.964	0.965	0.963	0.968	0.970	0.975
	40	1.342	1.343	1.343	1.347	1.351	1.359
	50	1.722	1.720	1.723	1.722	1.724	1.728

Table 3: Maximum displacements for each simulation

Chapter 6: Discussion

The model used in this study was developed as a result of CT examination of a healthy skull. This model was subjected to various forces that could be expected to manifest in a fall situation to determine the reaction of the skull, and by proxy, the brain, to the situation. The stress values evoked in the elements of the skull showed large variance between the different simulations. The minimum stress value of 13.95 MPa was found for the frontal test with the lowest maximum force value and the lowest maximum load rate. Likewise, the maximum stress value of 94.97 MPa was found in the lateral simulation with the highest load rate and maximum force values. These maximum values were found in close proximity across the different tests. Though there was a force development in the sphenoid during the lateral tests, as seen in figure 14, this only achieved 40% of the maximum force felt at the area of impact.

The results of these experiments were used to develop a mathematical prediction model for impacts to the front and lateral sides of the skull. Both least squares analysis and a neural network model were used to achieve equations relating input and output parameters for skull fracture. These models can subsequently be used for the analysis of injury chance due to deflection of, or stress creation in, the skull.

6.1. Least Squares Analysis of the Effect of Maximum Load on Maximum Stress

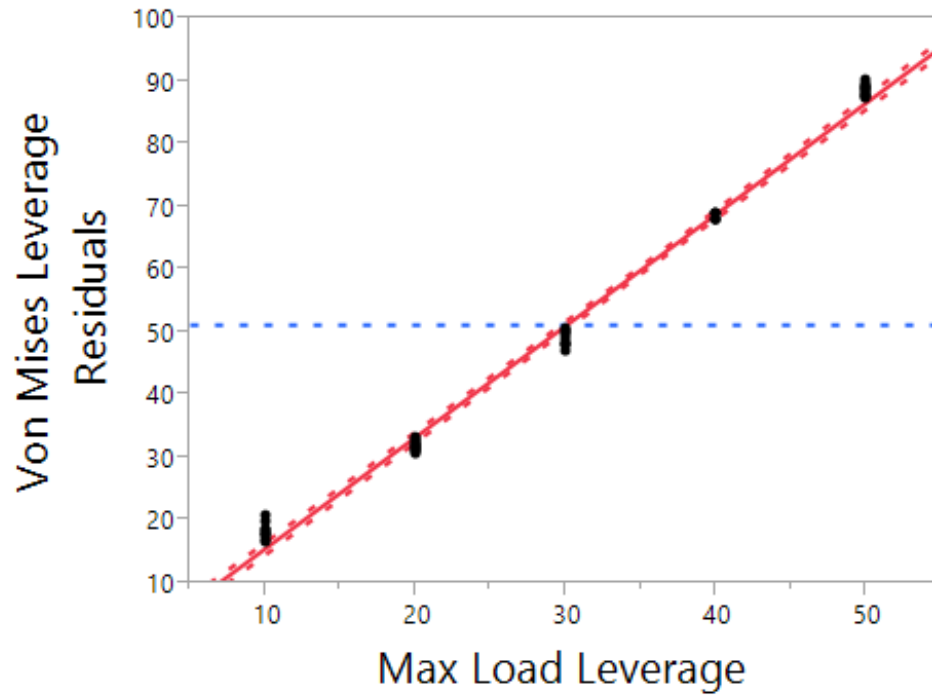


Figure 19: Leverage test of maximum load (kN) on the maximum stress (MPa) evoked in the simulation.

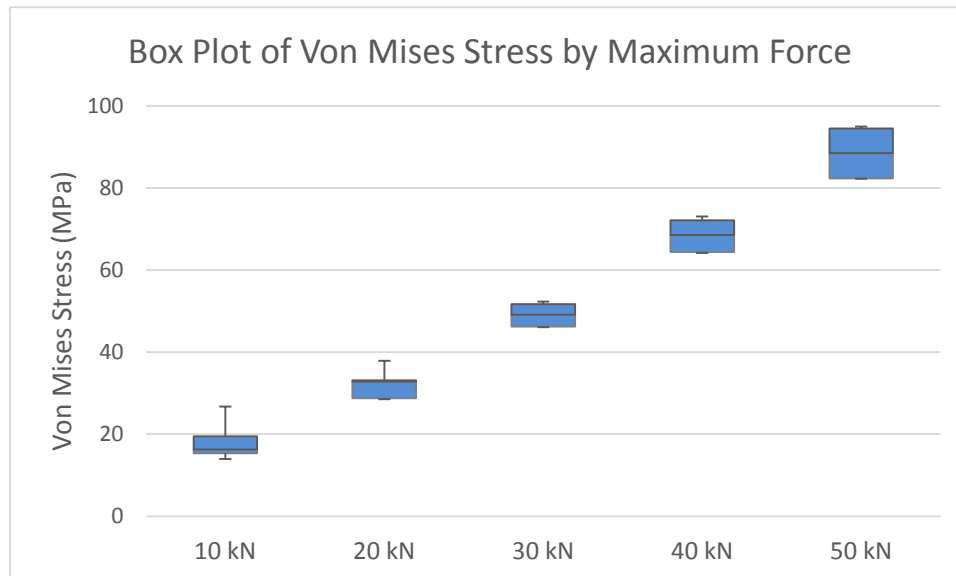


Figure 20: Box and whisker plot of maximum force values on von Mises stress.

Least squares analysis showed that maximum load's effect on the stress values produced was significant ($P < 0.0001$). Figure 19 shows the leverage effect tests for the von Mises results with respect to the input maximum force values. Figure 20 shows the box and whisker plot representation of the von Mises data produced from changing the input force values. All of the maximum force values show significant differences from each other, although the upper quartile of the 10 kN test is about 1.5 standard deviations from the lower quartile of the 20 kN test. The maximum stress found in the skull was found to increase as the maximum load rate increased. The maximum stress increased by 494% when increased from 10 to 50 kN. This is 6% under what would be expected if the stress response was linear in nature from 0 to 50 kN. More of a discrepancy can be seen at lower force values. The increase of force from 10 to 20 kN was equal to 178%, which is 22% less than the expected, following a direct, linear analysis.

6.2. Least Squares Analysis of the Effect of Load Rate on Maximum Stress

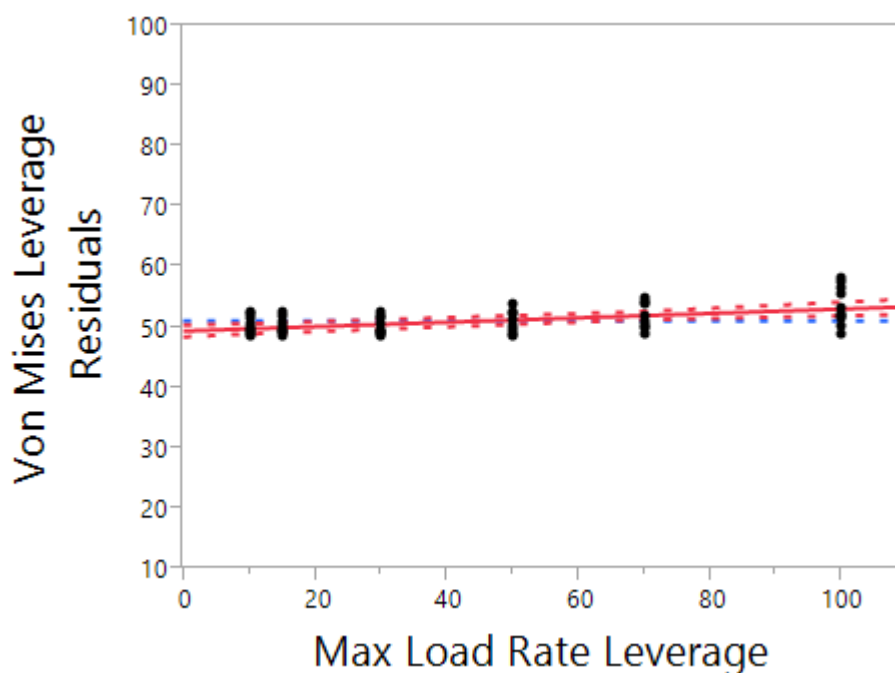


Figure 21:
Leverage test of
maximum load
rate (kN/ms) on
the maximum
stress (MPa)
evoked in the
simulation.

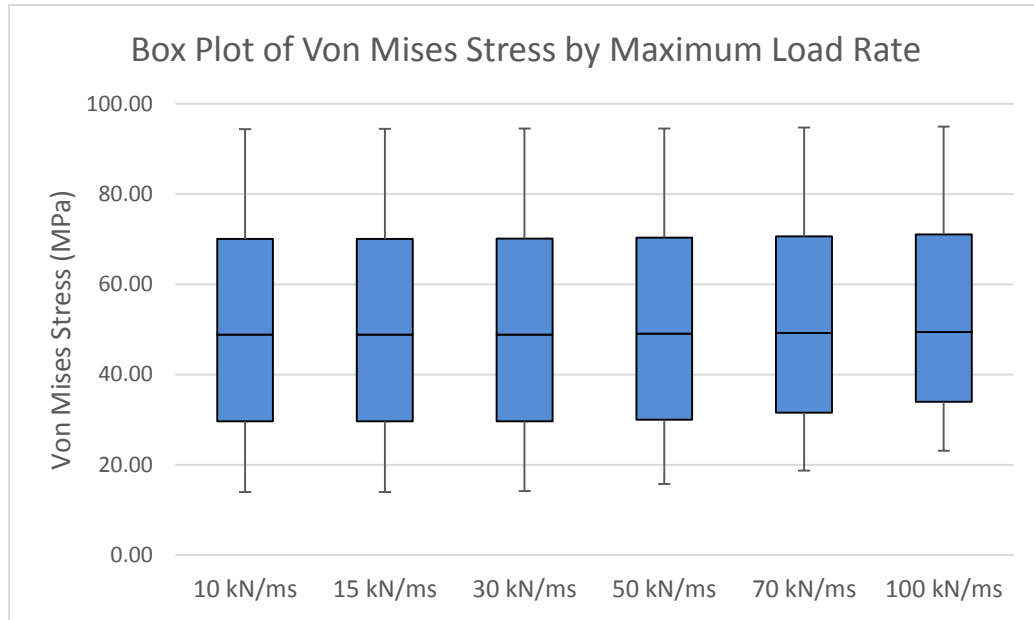


Figure 22: Box and whisker plot of maximum loading rate values on von Mises stress.

Least squares analysis showed that the load rate was significant in determining stress produced by the model ($P < 0.0001$). Figure 21 shows the leverage effect tests for the von Mises results with respect to the input load rate values. Though this graph shows the von Mises stress increases corresponding with maximum load rate, and while a diminished effect on the von Mises stress is seen when compared to the maximum load, it still shows a scientifically significant impact upon the calculation. Figure 22 shows the box and whisker plot representation of the von Mises data produced from changing the input force values. While none of the individual plots show a significant change between the relative values in this diagram, the increasing value of the bottom quartile with increasing load rate shows a change across the diagram that is not reflected in the rest of the data points. The ordered nature of this increase indicates for an interaction of the maximum load rate with another of the input variables, which will be addressed in the predictive model section of this paper. Though not significant on the box and whisker

plot, when filtered in least squares analysis, a 6.54% increase in the von Mises stress was seen when comparing the 100 and 10 kN/ms maximum load rate means. As with the maximum load, this did not show a strictly linear increase, with a 0.176% increase from 10 to 15 kN/ms.

6.3. Least Squares Analysis of the Effect of Strike Location on Maximum Stress

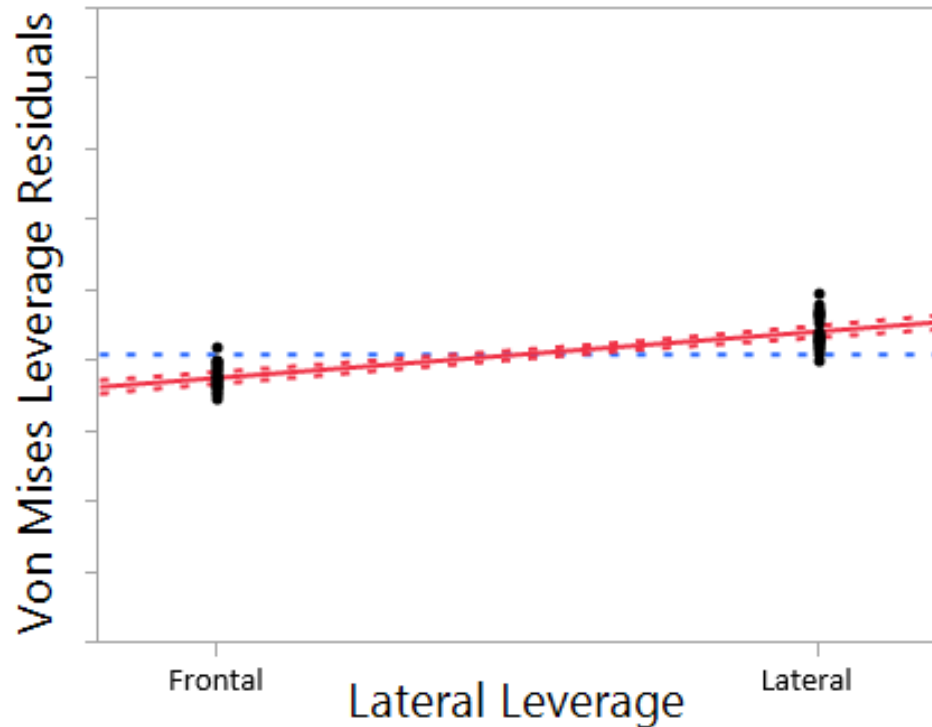


Figure 23: Leverage test of location on maximum stress evoked in simulation

Least squares analysis showed that the area of impact was significant in determining stress produced by the model ($P < 0.0001$). Figure 23 shows the leverage effect tests for the von Mises results with respect to the strike location. This shows that the lateral location shows a higher stress formation than does the frontal. By itself, this does not imply that either location have a greater or diminished capacity for absorbing stress before a fracture. Figure 23 shows the box and whisker plot from this diagram, based on a change in impact location. As with the maximum load rate, the box plots cannot distinguish the differences due to location by themselves; although they do qualitatively indicate for a uniform change in the stress experienced when inputting in variables. The lateral bones experienced a 14.0% increase in stress compared to the frontal bones. This increase can be used to compare strikes to aforementioned points, but because location is an ordinal variable rather than a numerical input, the transfer function that connects these points cannot be commented upon further.

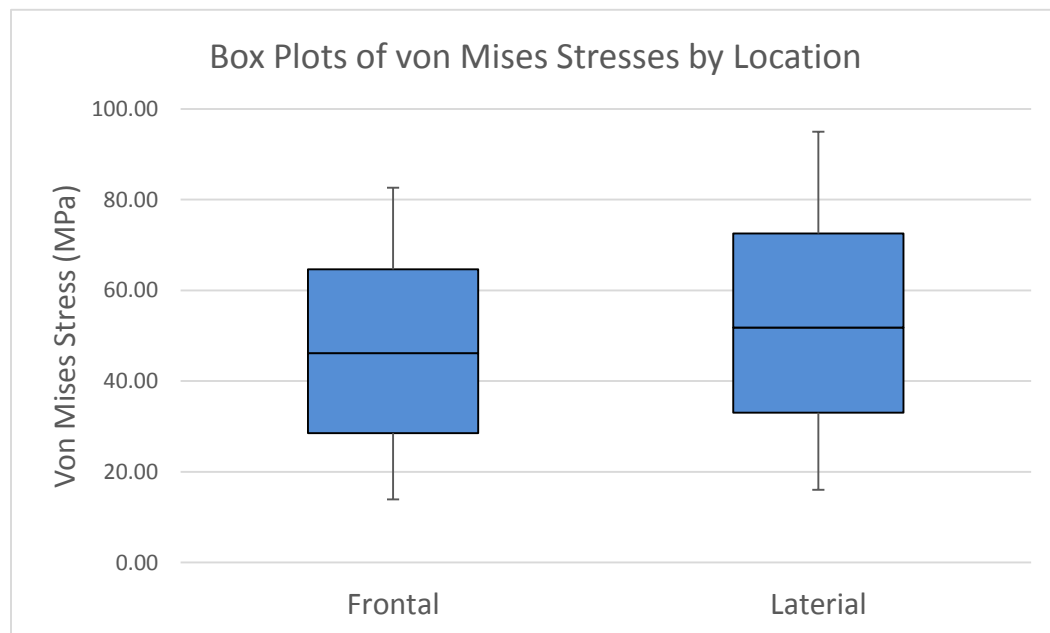


Figure 24: Box and whisker plot of the location on von Mises stress

6.4. Least Squares Analysis of the Combination Terms on Maximum Stress

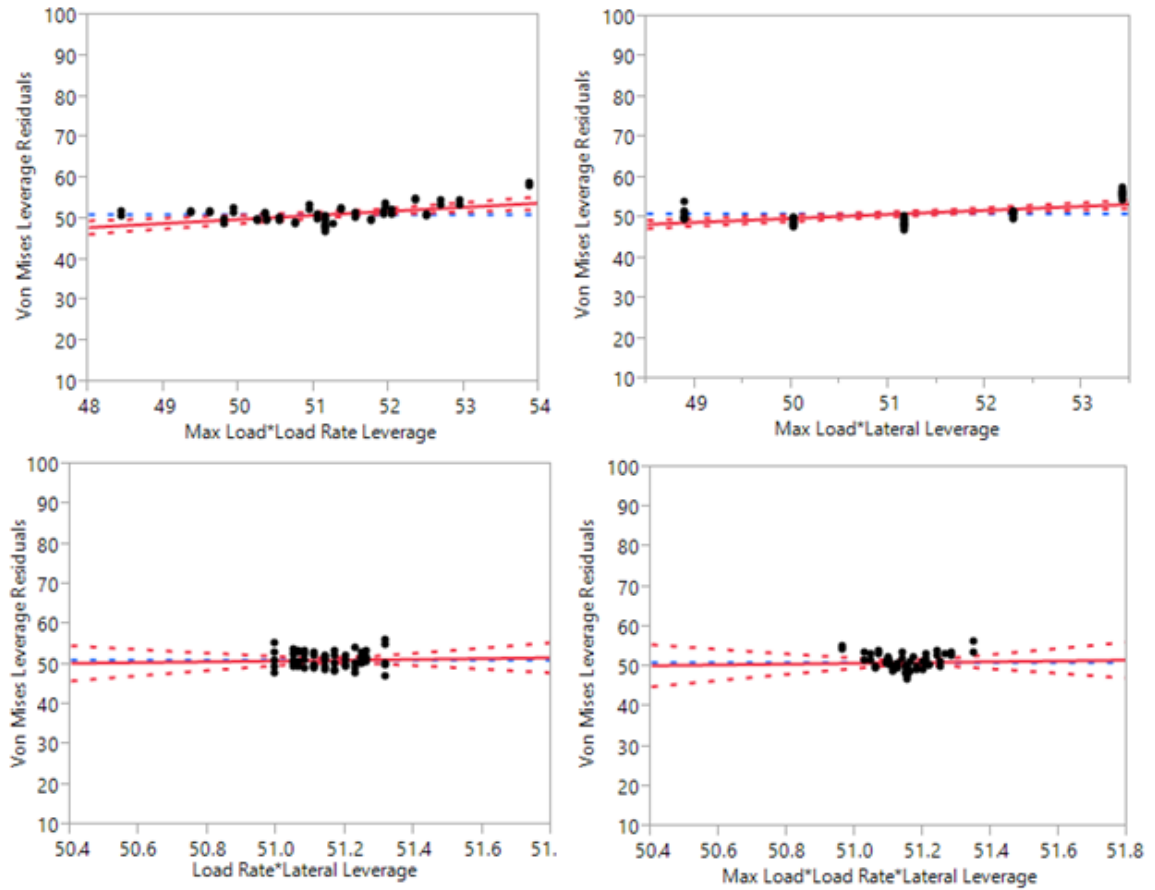


Figure 25: Leverage test for various input variables on maximum stress evoked in simulation. Tests from top left, clockwise; (max load)*(load rate), $P=0.0001$; (max load)*(location), $P<0.0001$; (max load)*(load rate)*(location), $P=0.7737$; (load rate)*(location), $P=0.7300$.

Using least squares analysis, the combination terms of (maximum load)*(maximum load rate), (maximum load)*(location), (maximum load)*(maximum load rate)*(location), and (maximum load rate)*(location) were all analyzed. (Maximum load)*(maximum load rate) was significant at $P=0.0001$. (Maximum load)*(location) was significant at $P<0.0001$. (Maximum load)*(maximum load rate)*(location) was not

significant at $P=0.7737$. (Maximum load rate)*(location) was not significant at $P=0.7300$.

Leverage plots of these statistics can be seen in figure 25. As it can be seen, all four of these have a smaller effect on the stress than the maximum load rate, but (maximum load)*(maximum load rate) and (maximum load)*(location) are still statistically significant effects. A graphical depiction of the effects that these variables have in relation to each other can be seen in figure 26. Based on these results, it can be seen that

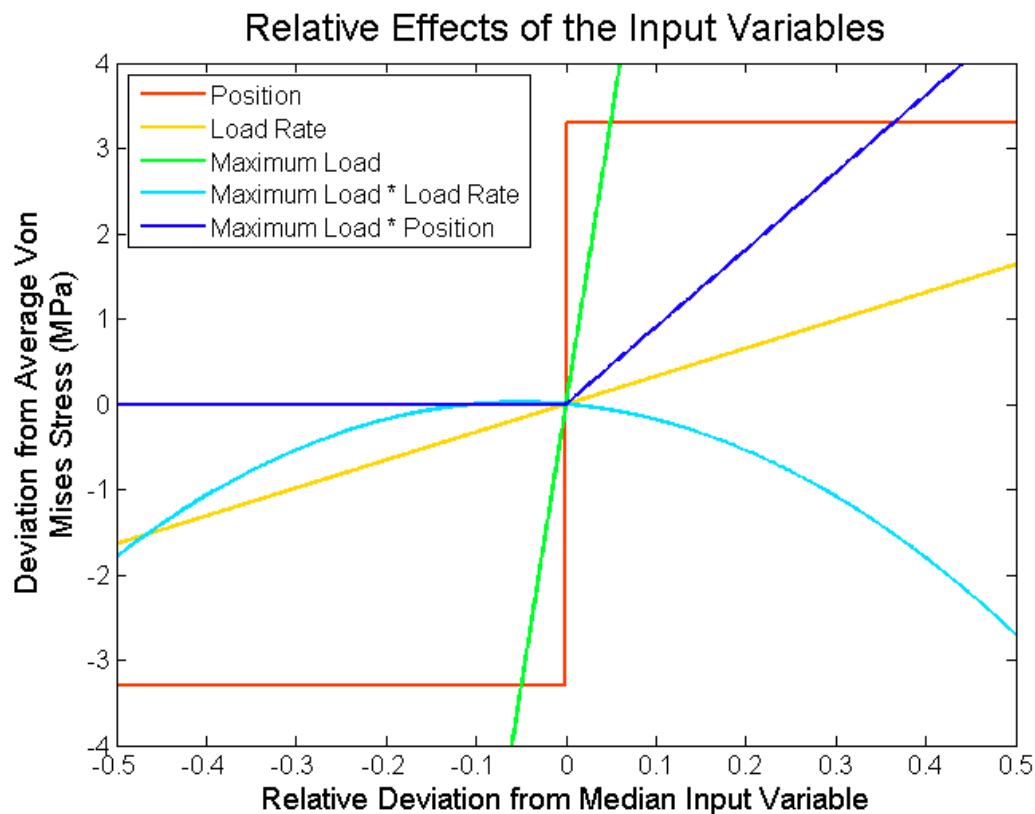


Figure 26: Relative scale of the effects of the input variables on von Mises stress based on least squares analysis. All variables were scaled from their minimum and maximum inputs to fit from -0.5 to 0.5. For example, -0.5 corresponds to the minimum load rate of 10 kN/ms, while 0.5 corresponds to a load rate of 100 kN/ms.

each factor influences the von Mises stress in a different way. As to be expected given the results seen previously, maximum force and load rate cause the von Mises stress to increase over time, although an increase in the maximum force causes a more pronounced

effect over the ranges used here. Additionally, as to be expected given that position is an ordinal variable, the effect of changing location is manifested as a step function. Load crossed with load rate causes the effect decreasing the von Mises stress as values move from the median input value. The peak von Mises stress seen from this term is at -0.052, which corresponds to a maximum load of 27.9 kN and a maximum load rate of 50.1 kN/ms. The other term, load crossed with position, displays an increase in the von Mises stress for impacts on the lateral side of the skull, but not for the frontal region. The profile created by this curve has to do with the effects of the geometry of the skull as well as the ordinal nature of the location input upon stress formation.

6.5. Least Squares Prediction Equation for Stress Values

Combining all of these results yielded the general equation shown in equation 4, which was a linear combination of terms for the maximum von Mises stress. Maximum load, maximum load rate, and location were the input parameters. This equation was developed between a maximum load of 10 to 50 kN and a maximum load rate of 10 to 100 kN. Impacts to the frontal region use a value of 0 in the case functions and lateral impacts use a 1. As mentioned previously, because experimentation was not able to be done on a continuum of points, the location parameter should be treated as an ordinal variable.

Maximum von Mises Stress

$$\begin{aligned}
 &= -3.714 + 1.6633 * (Max\ Load) + 0.03643 * (Load\ Rate) \\
 &- 0.002502 * (Max\ Load - 30) * (Load\ Rate - 45.83) + 6.599 \\
 &* \begin{cases} Lateral = 1 \\ Frontal = 0 \end{cases} + 0.2263 * (Max\ Load - 30) \\
 &* \begin{cases} Lateral = 1 \\ Frontal = 0 \end{cases} \dots \dots \dots (4)
 \end{aligned}$$

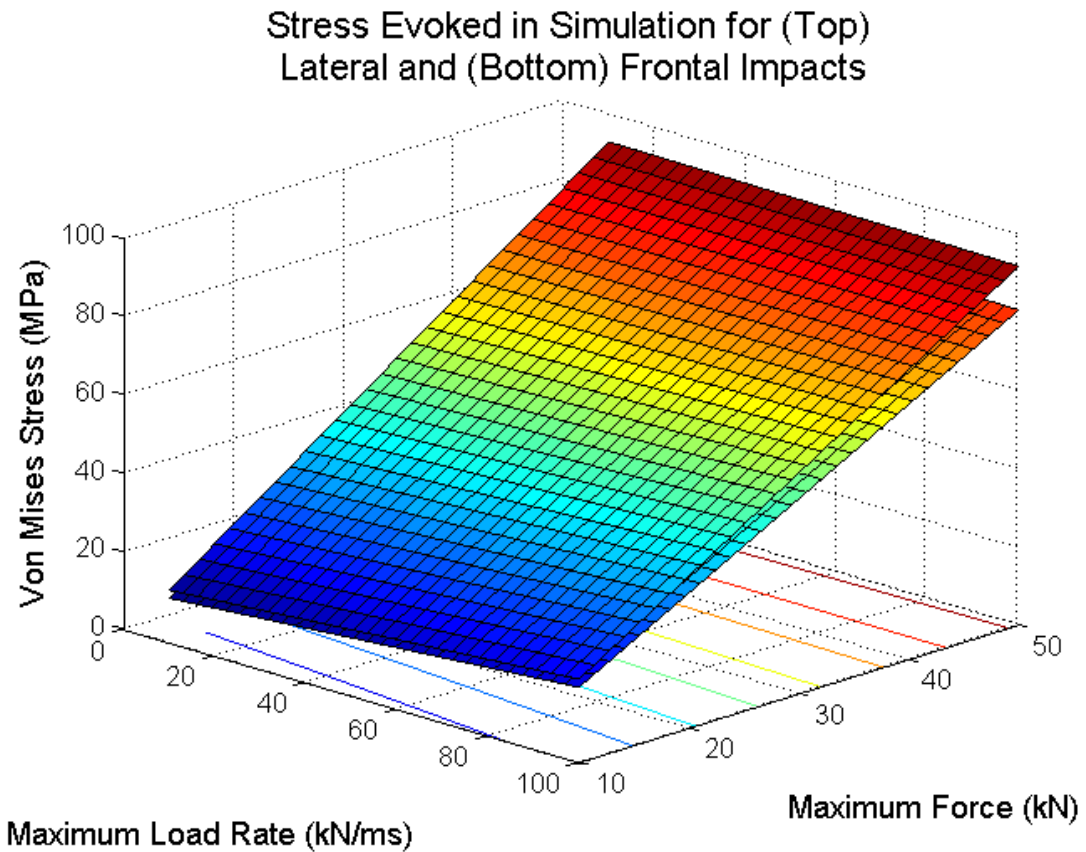


Figure 27: Stress values predicted by least squares method from simulation. Note the contour lines askew from the maximum force lines, demonstrating effect of the load rate.

Inputs for maximum load are kN and inputs for maximum load rate are kN/ms. Output is in units of MPa. This equation has an adjusted R^2 value of 0.994, implying good fit of the data. It is shown graphically in figure 27. The lowest predicted value using the boundaries of the input parameters was at maximum load rate = 10 kN/ms, maximum load = 10 kN, and frontal analysis. This yielded a maximum stress value of 13.95 MPa, compared to the lowest recorded value of 11.49 MPa. Similarly, a maximum predicted value at load = 50 kN, load rate = 100 kN/ms, lateral mode gave a prediction of 91.52 MPa compared to the observed 94.97 MPa. A plot of the residuals of the prediction

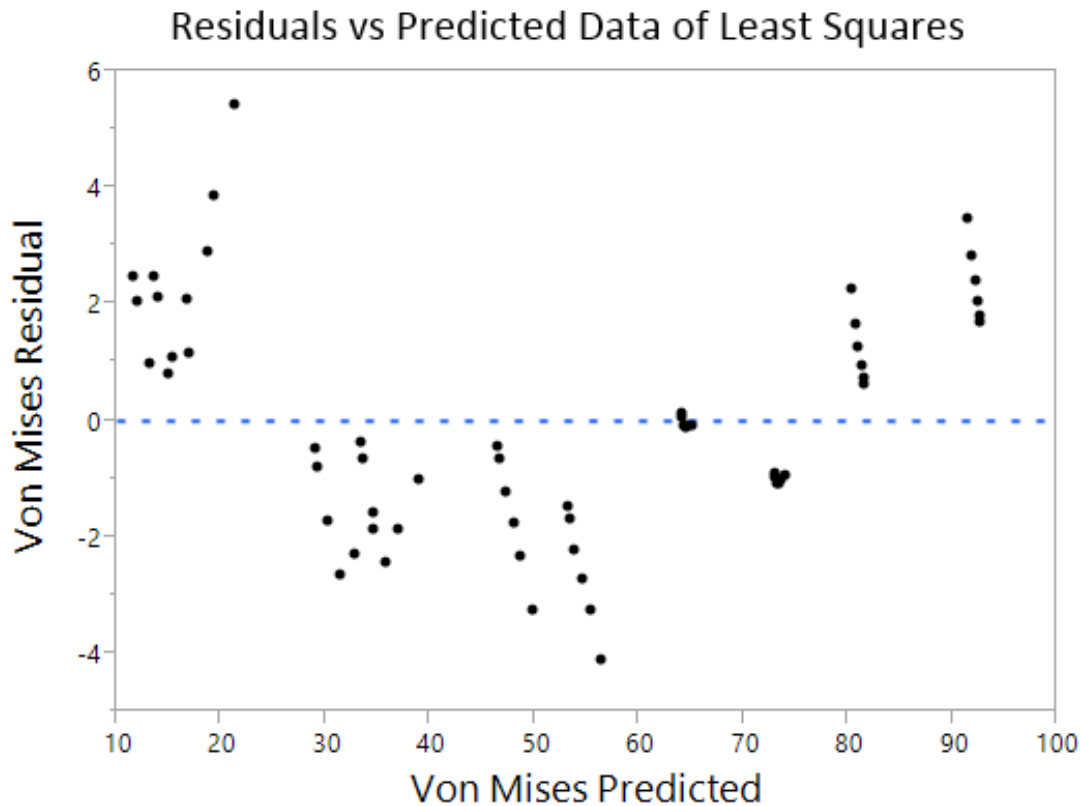


Figure 28: Plot of the residuals of the least squares analysis against the fitted data. The data appears to be following an additional parabolic function in this analysis, which is not accounted for due to the linear nature of the predictive formula.

equation to the fitted data is viewable in figure 28. Based on the residuals, while the linear analysis of stress data is a good approximation to the data, it is not able to capture the non-linear effects shown in figure 28.

$$\text{Maximum von Mises Stress} = -2.139 + 1.776 * (\text{Maximum Load}) \dots \dots (5)$$

In addition to the linear equation shown in equation 4, a simpler formula is shown in equation 5, which had an adjusted R^2 value of 0.971, still showing a relatively good fit of the data. Using the same minimum and maximum values, a minimum value of 15.62 MPa and a maximum of 86.66 MPa were found. While this is not as sensitive to the input conditions as equation 4, it utilizes only the maximum load input, from which the majority of stress values are evoked. This simplifies the equation while still maintaining a somewhat reliable fit. Additionally, because this only removes input terms which add to the completeness of equation 4, the simplification here still suffers from the same issues as equation 4. This includes the nonlinear residual data found in the equation.

6.6. Neural Network Analysis for Stress in the Skull

Neural network analysis of data provides a more accurate fit to the data in question. It has a possibility of overfitting the data however by including random noise and by diverging when extrapolating from the input parameters. Because the in silico finite element model here has a limited amount of noise when compared to laboratory conditions of testing, neural network modeling is an accurate and reliable method of determining a predictive equation.

A neural network was created using the holdback method with a holdback proportion of 0.3333 and 3 hidden nodes which accept the initial variables and apply a transfer function before combining the results, as seen in figure 29. This divides the data randomly into two different sets; one set used to create the model

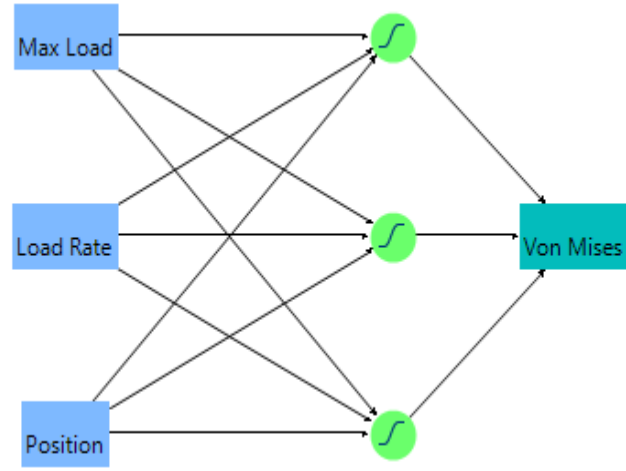


Figure 29: Diagram of the mechanism of a neural network, showing the hidden nodes which combine

and the second used to validate it to avoid overfitting of the data. This created an initial model of the data with an R^2 value of 0.9997. It was then validated at 0.9990, showing a better fit of the data than shown in the least squares analysis. This equation was developed between a maximum load of 10 to 50 kN and a maximum load rate of 10 to 100 kN. Impacts to the frontal or lateral regions use the value designated in their choice functions. Again, location should be treated as an ordinal parameter. The neural network equation can be seen in equation 6.

$$Von\ Mises\ Stress = 52.169 - 37.360 * H1 + 13.736 * H2 + 54.0320 * H3;$$

$$H1 = TanH \left(0.5 * \left(1.8063 - 0.05863 * (Max\ Load) + 0.01155 * (Load\ Rate) - \begin{cases} Frontal = 0.03445 \\ Lateral = -0.03445 \end{cases} \right) \right)$$

$$H2 = TanH \left(0.5 * \left(-2.1286 + 0.1090 * (Max Load) + 0.01235 \right. \right.$$

$$\left. * (Load Rate) + \begin{cases} Frontal = 3.9476 \\ Lateral = 3.9476 \end{cases} \right)$$

$$H3 = TanH \left(0.5 * \left(-0.9928 + 0.02908 * (Max Load) + 0.007772 \right. \right.$$

$$\left. * (Load Rate) - \begin{cases} Frontal = 0.6122 \\ Lateral = 0.6122 \end{cases} \right) \dots \dots \dots (6)$$

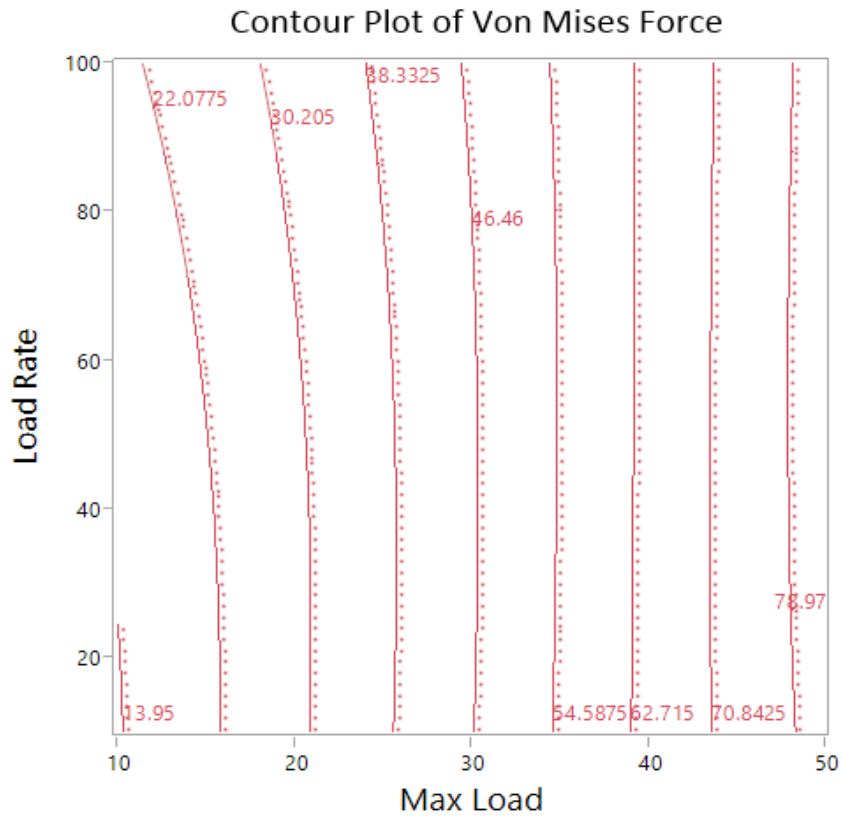
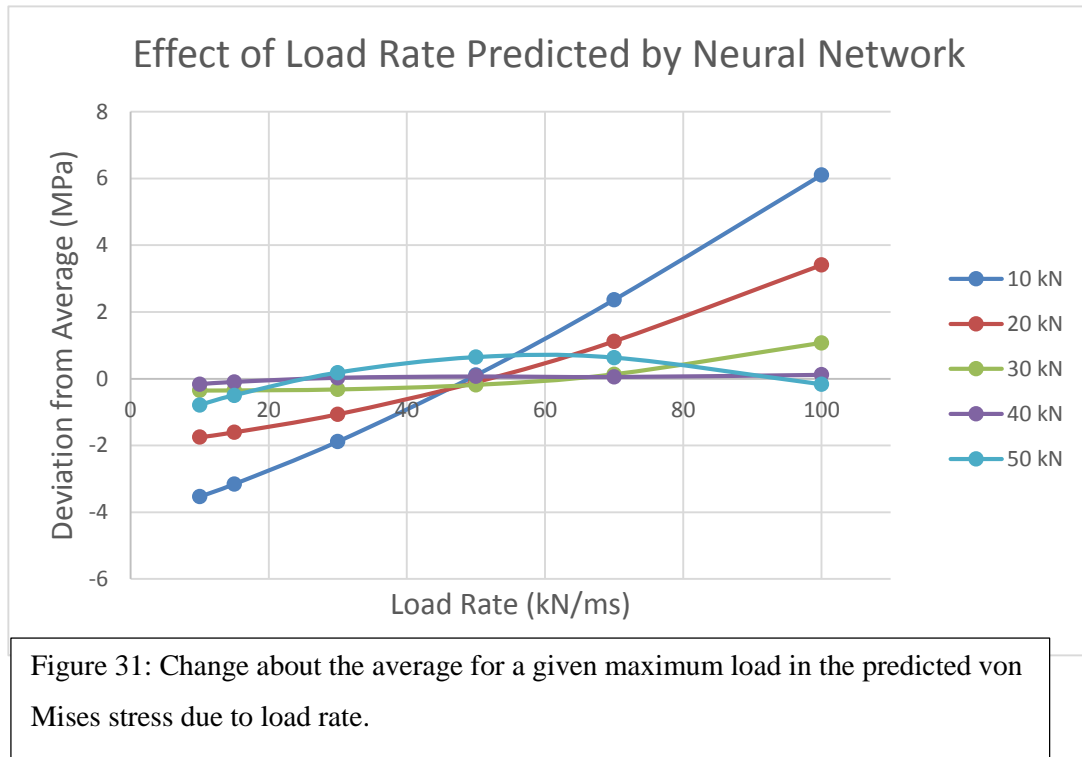


Figure 30: Contour plot of the Von Mises stress from neural network with respect to maximum load and load rate. Contours are lines of the specified von Mises value.

Inputs for maximum load are kN and inputs for maximum load rate are kN/ms. Output is in units of MPa. This model, while daunting at first glance, is easily used in computation. Effect testing for the model gives weights for the importance of variables in contributing to the overall effect. Maximum load had a relative effect of 0.484, position had an effect of 0.013, and load rate had an effect of 0.003. Though diminished compared to the maximum load, the effect of the load rate and its decreasing effect with greater maximum loads is still clearly visible in figure 30.



The lowest predicted value using the boundaries of the input parameters was at maximum load rate = 10 kN/ms, maximum load = 10 kN, and frontal analysis. This yielded a maximum stress value of 13.56 MPa, compared to the lowest recorded value of 13.95 MPa. This was more accurate than the least squares value by a factor of 6.3. A

maximum predicted value at load = 50 kN, load rate = 50 kN/ms, lateral mode gave a prediction of 95.20 MPa compared to the observed 94.97 MPa. This also gave a more accurate result to the observed maximum when compared to least squares, by a factor of 15. Because of the more complicated steps in the neural network, the predicted von Mises stress was found to decrease for the 50 kN maximum load test when the load rate exceeded 50 kN/ms. A plot of the von Mises stresses centered about the average point by load rate can be seen in figure 31. Examination of this diagram shows that negative derivatives for load rate can be seen at this point as well as the 50 kN load, 70 kN/ms

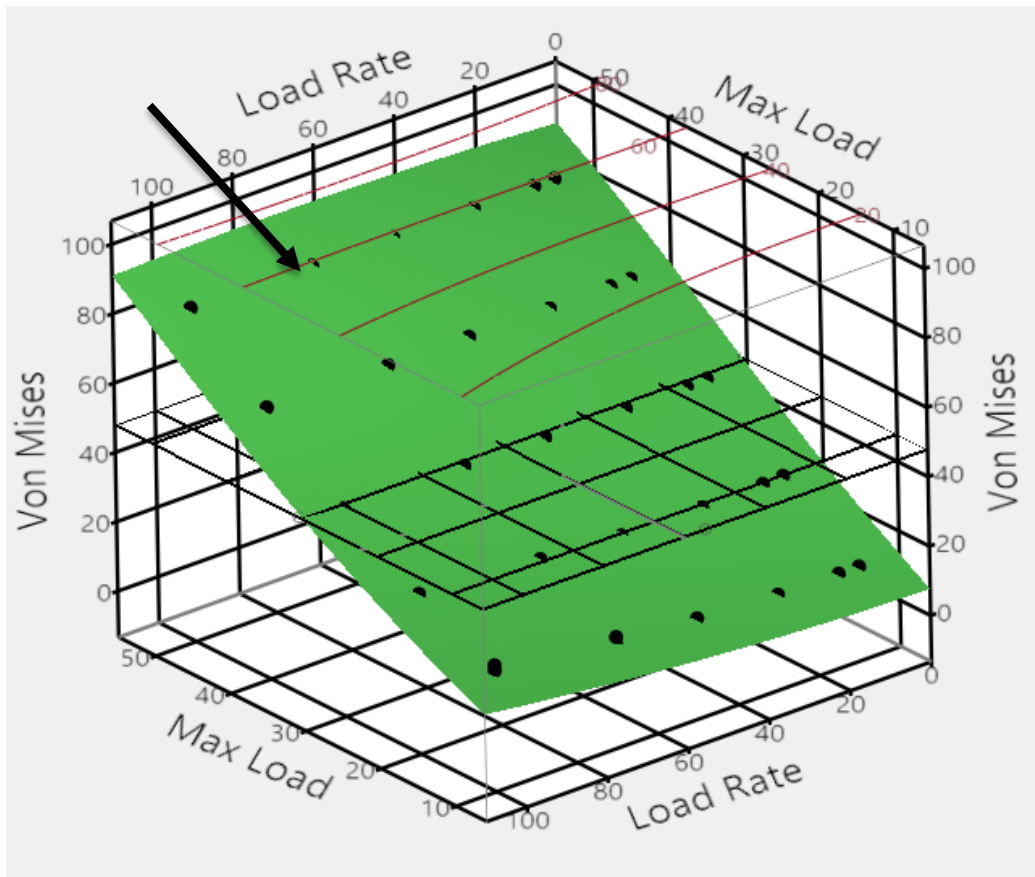


Figure 32: Plot of residuals of the neural network model. Contour lines can be seen on the top of the diagram. Arrow pointing towards hump in the model (shown by sunken residuals), where peak was found in the load rate.

load rate and the 40 kN, 70 kN/ms load rate points. All other locations show increasing von Mises stresses with respect to load rate. This peak is probably an artifact of the holdback process of model creation and, despite it, the neural network model is still a very good fit for the data when used within the input parameter ranges. A plot of the residuals of the prediction equation to the fitted data is viewable in figure 32.

6.7. Maximum Deflection

In the same way that stress was measured, deflection was analyzed. While stress can be used as an indicator for skull fracture, which points to a high incidence of traumatic brain injury, deflection of the skull can place pressure on the brain. It is well known that the skull is capable of such bending, with minor examples of flexion found to accommodate blood flow and examples of more pronounced flexion in head injury – especially blast related modalities. Should the deflection of the skull reach a high enough value, it can cause injury without skull fracture occurring. The minimum deflection value of 0.29 mm was found for the frontal test with the lowest maximum force value and the lowest maximum load rate. Likewise, the maximum deflection value of 1.98 mm was found in the lateral simulation with the highest load rate and maximum force values. These experiments were used to develop a mathematical prediction model for impacts to the front and lateral sides of the skull. Both least squares analysis and a neural network model were used to achieve equations relating input and output parameters for skull fracture. These models can subsequently be used for the analysis of injury chance due to deflection of, or stress creation in, the skull.

6.8. Least Squares Analysis of the Effect of Maximum Load on Deflection

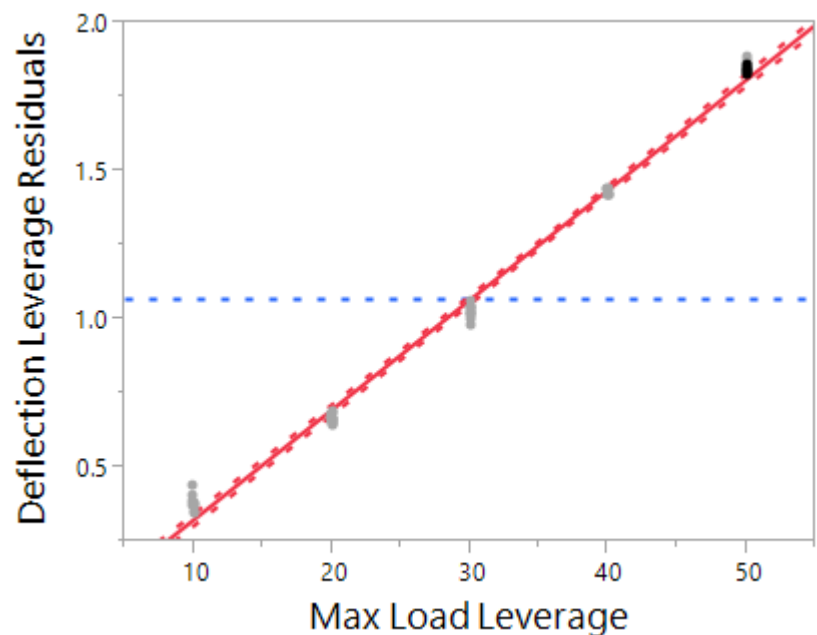


Figure 33: Leverage test of maximum load on deflection evoked in simulation.

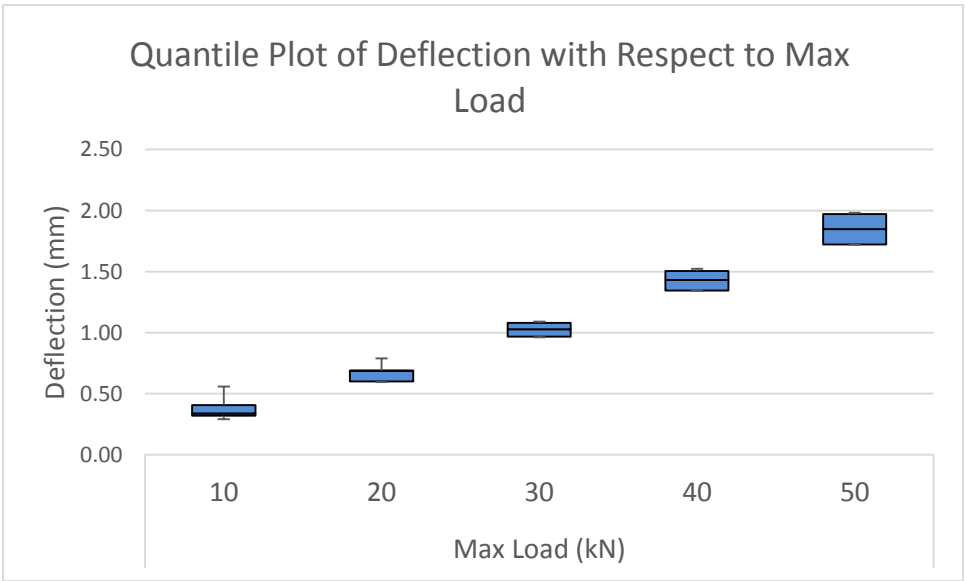


Figure 34: Box and whisker plot of maximum force on displacement.

Least squares analysis showed that the maximum load was significant in determining stress produced by the model ($P < 0.0001$). Figure 33 shows the leverage effect tests for the von Mises results with respect to the load. As could be expected, as the force increased, the amount of deflection increased proportionally. Figure 34 shows the box and whisker plot representation of the deflection data produced from changing the input force values. As with the stress measurement, all of the maximum force values show significant differences from each other. The maximum deflection found in the skull was found to increase as the maximum load rate increased. The deflection also increased by 494% when increased from 10 to 50 kN, similar to the stress test.

6.9. Least Squares Analysis of the Effect of Load Rate on Deflection

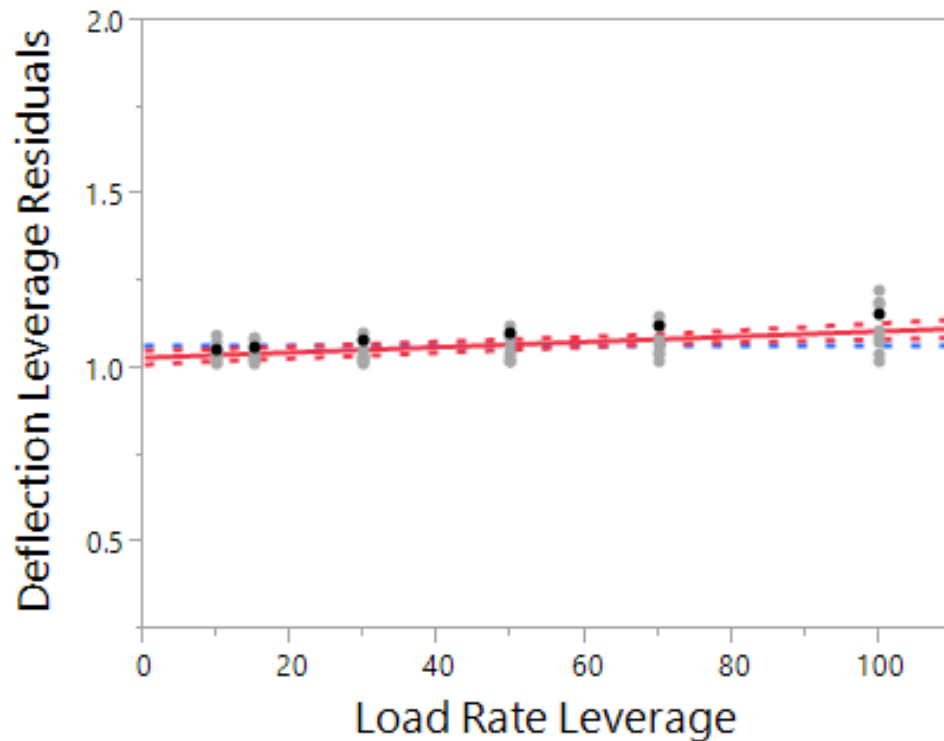


Figure 35: Leverage test of maximum load rate on the deflection evoked in the simulation.

Least squares analysis showed that the load rate was significant in determining deflection produced by the model ($P < 0.0001$). Leverage test can be seen in figure 35, and a box and whisker plot in figure 36. As the effects tests of maximum load on displacement were similar to the effect of load on stress, so to were the tests for load rate similar. Deflection was found to increase with load rate. When examined in least squares analysis, a 6.55% increase in the von Mises stress was seen when comparing the 100 and 10 kN/ms maximum load rate means. This shows a slight difference (0.01%) in the increase as compared with the similar increase in von Mises stress. Furthermore, the non-linear progression of the displacement was seen, with a 0.167% increase from 10 to 15 kN/ms, differing from the 0.176% increase in stress values.

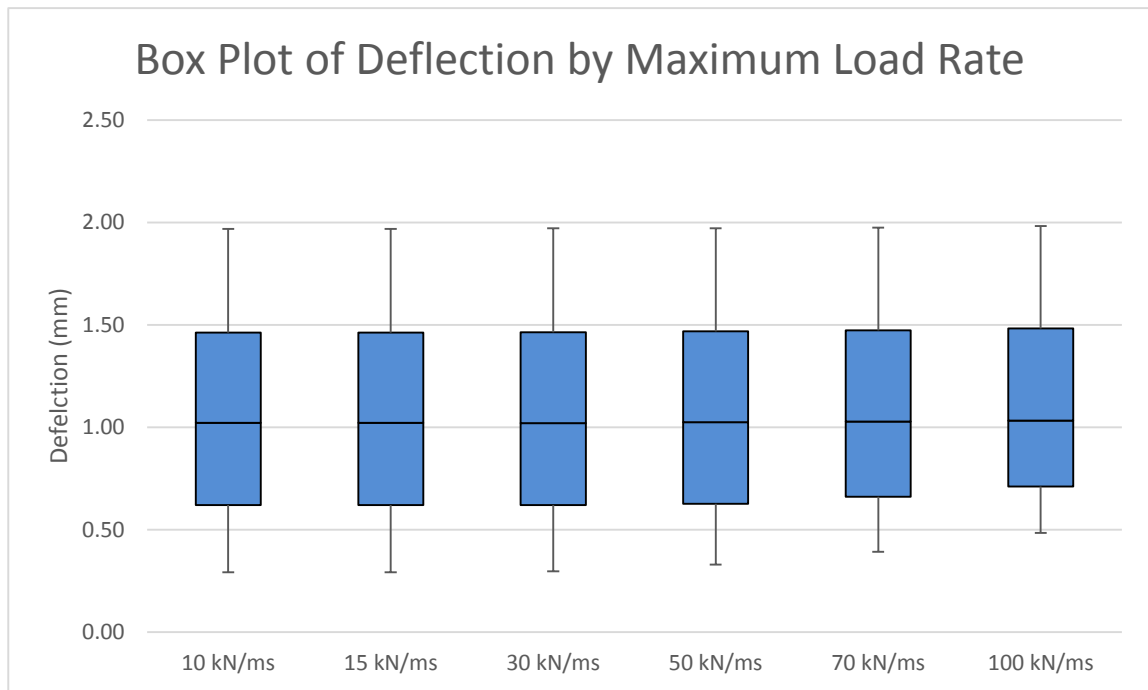


Figure 36: Box and whisker plot of load rate on displacement.

6.10. Least Squares Analysis of the Effect of Strike Location on Deflection

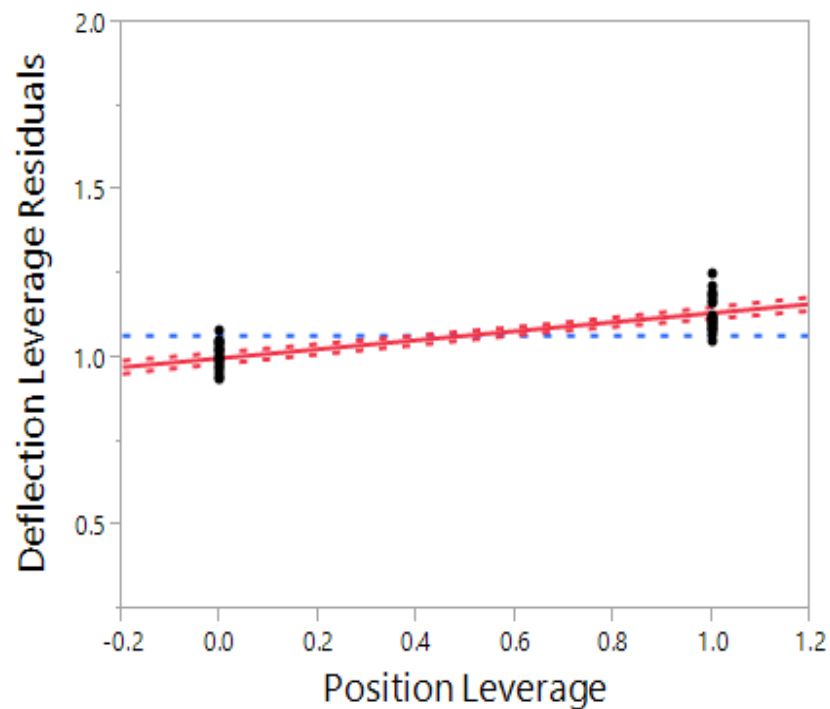


Figure 37: Leverage test of impact location on deflection evoked in simulation

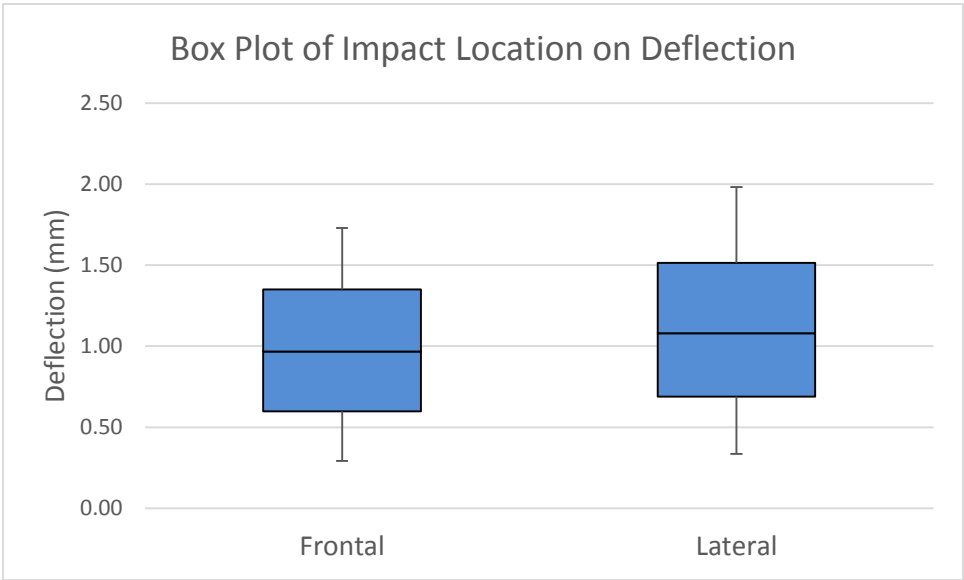


Figure 38: Box and whisker plot of impact location on displacement

Least squares analysis showed that the area of impact was significant in determining deflection produced by the model ($P < 0.0001$). Figure 37 shows the leverage effect tests for the deflection results with respect to the strike location. This shows that the lateral location shows a higher deflection than does the frontal. Figure 38 shows the box and whisker plot from this diagram, based on a change in impact location. The lateral bones experienced a 13.5% increase in deflection compared to the frontal bones, compared to a 14.0% increase in stress. Once again, this category should be treated as an ordinal variable, and one should not assume the transfer function between these variables.

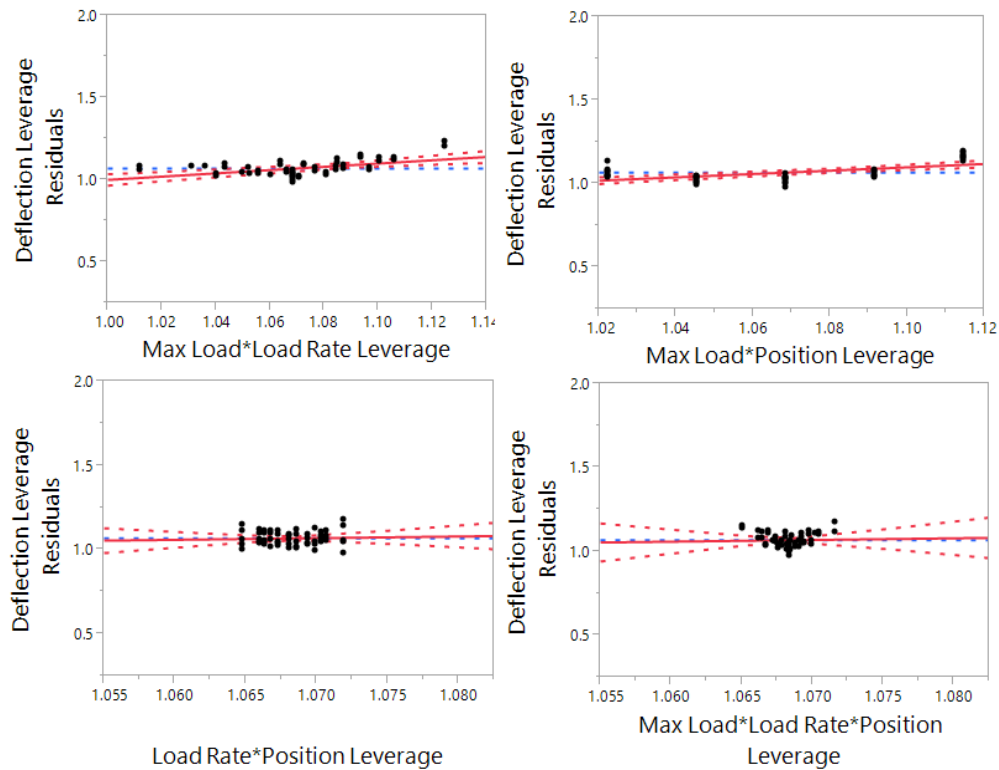


Figure 39: Leverage test for various input variables on maximum stress evoked in simulation. Tests from top left, clockwise; (max load)*(load rate), $P=0.0002$; (max load)*(location), $P<0.0001$; (max load)*(load rate)*(location), $P=0.8137$; (load rate)*(location), $P=0.7152$.

6.11. Least Squares Analysis of the Effect of Combination Terms on Deflection

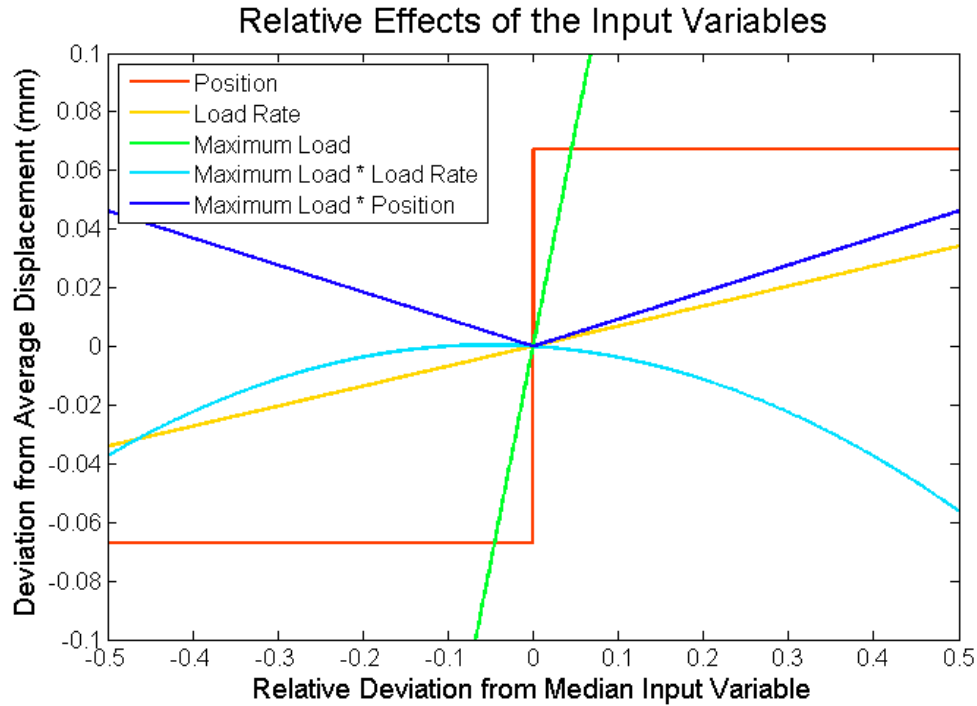


Figure 40: Relative scale of the effects of the input variables on displacement based on least squares analysis. All variables were scaled from their minimum and maximum inputs to fit from -0.5 to 0.5. For example, -0.5 corresponds to the minimum load rate of 10 kN/ms, while 0.5 corresponds to a load rate of 100 kN/ms.

Using least squares analysis, the combination terms of (maximum load)*(maximum load rate), (maximum load)*(location), (maximum load)*(maximum load rate)*(location), and (maximum load rate)*(location) were all analyzed. (Maximum load)*(maximum load rate) was significant at $P=0.0002$. (Maximum load)*(location) was significant at $P<0.0001$. (Maximum load)*(maximum load rate)*(location) was not significant at $P=0.8137$. (Maximum load rate)*(location) was not significant at $P=0.7152$. Leverage plots of these statistics can be seen in figure 39. As for the stress values, all four of these have a smaller effect on the stress than the maximum load rate, but (maximum

load)*(maximum load rate) and (maximum load)*(location) are still statistically significant effects. A graphical depiction of the effects that these variables have in relation to each other can be seen in figure 40. As with the calculations for stress, each factor influences the displacement in a different way. Maximum force and load rate both cause the displacement to increase over time and the position effect is a step function, as per previous results. Load crossed with load rate causes the effect decreasing the displacement as values move from the median input value. The peak deflection seen from this term is at -0.052, which corresponds to a maximum load of 27.9 kN and a maximum load rate of 50.1 kN/ms. This is also consistent with the stress values, which implies that this and the previous terms are simply a differently weighted version of the term or the stress calculations. The other term, load differs from crossed with position, displays an increase in the displacement for impacts on the lateral side of the skull, and a slightly greater increase for the frontal side when compared to the deflection experienced at the zero point of the adjusted variables for (load)*(position). The profile created by this curve has to do with the effects of the geometry of the skull as well as the ordinal nature of the location input upon displacement formation.

6.12. Least Squares Prediction Equation for Deflection

Combining all of these results yielded the general equation shown in equation 7, which was a linear combination of terms for the maximum deflection. Maximum load, maximum load rate, and location were the input parameters. This equation was developed between a maximum load of 10 to 50 kN and a maximum load rate of 10 to 100 kN. The

value used for impact location should be looked up in the choice functions shown in the equation. As mentioned previously, because experimentation was not able to be done on a continuum of points, the location parameter should be treated as an ordinal variable.

Maximum deflection

$$\begin{aligned}
 &= -0.1468 + 0.0371 * (Max\ Load) + 0.00075877 * (Load\ Rate) \\
 &- 0.00005205 * (Max\ Load - 30) * (Load\ Rate - 45.83) + 0.1346 \\
 &* \begin{cases} Lateral = 1 \\ Frontal = 0 \end{cases} + 0.004617 * (Max\ Load - 30) \\
 &* \begin{cases} Lateral = 0.5 \\ Frontal = -0.5 \end{cases} \dots \dots \dots (7)
 \end{aligned}$$

Inputs for maximum load are kN and inputs for maximum load rate are kN/ms. Output is in units of millimeters. This equation has an adjusted R^2 value of 0.993, implying good fit of the data. It is shown graphically in figure 41. The lowest predicted value using the boundaries of the input parameters was at maximum load rate = 10 kN/ms, maximum load = 10 kN, and frontal analysis. This yielded a maximum displacement of 0.1945 mm, compared to the lowest measured value of 0.292 mm. Similarly, a maximum predicted value at load = 50 kN, load rate = 100 kN/ms, lateral mode gave a prediction of 1.955 mm compared to the observed 1.983 mm. A plot of the residuals of the prediction equation to the fitted data is viewable in figure 42.

Maximum von Mises Stress

$$= -0.04468 + 0.0371 * (Maximum\ Load) \dots \dots \dots (8)$$

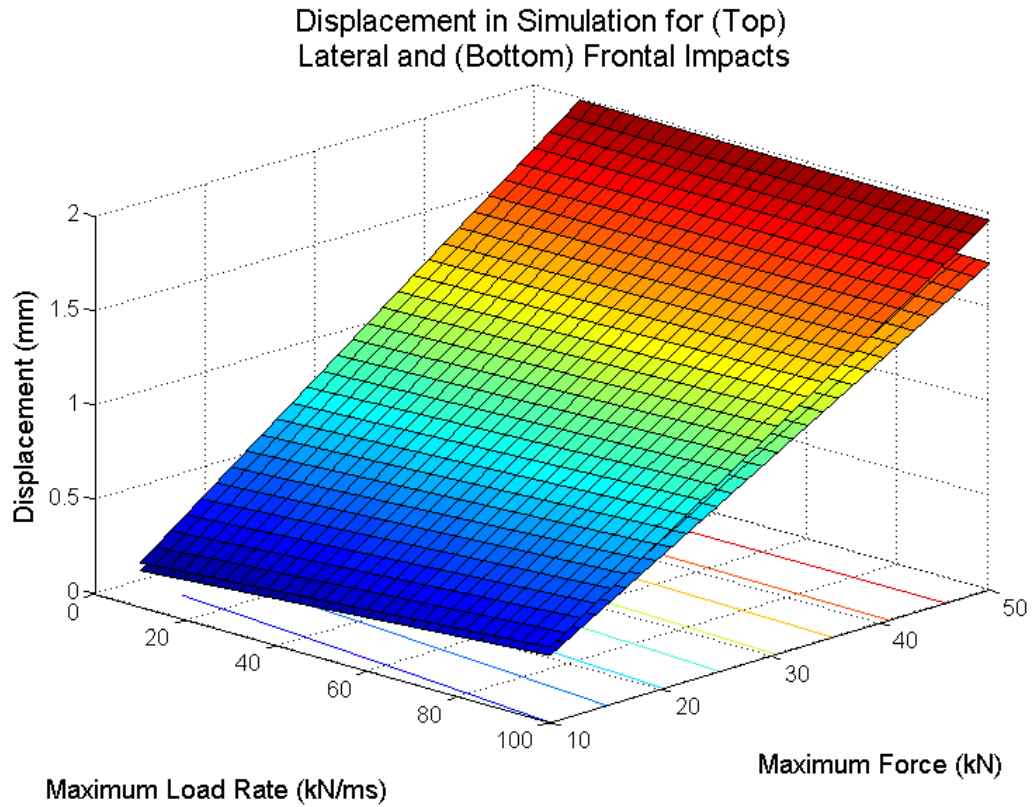


Figure 41: Displacement values as predicted by the least squares model for lateral and frontal impacts.

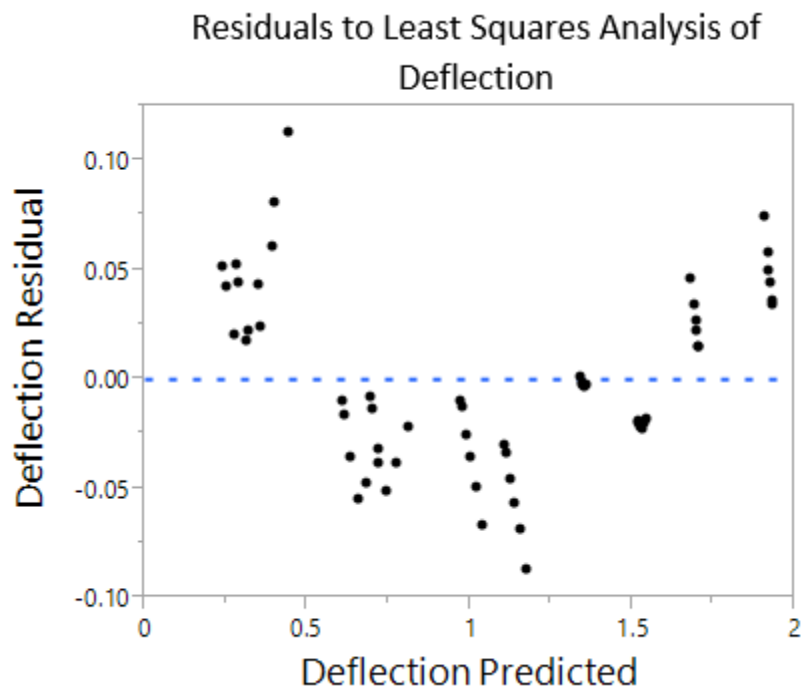


Figure 42: Plot of the residuals of the least squares analysis for deflection against the fitted data.

As maximum force was the most influential term on the analysis, a second formula containing only this term was created, which had an adjusted R^2 value of 0.970. This equation is shown in equation 8. Using the same minimum and maximum values for maximum load and load rate as used for equation 7, a minimum value of 0.3263 mm and a maximum of 1.810 mm were found. While this is not as sensitive to conditions as equation 7, it starkly approximates the input conditions while still achieving a reliable fit.

6.13. Neural Network Analysis for Deflection in the Skull

A neural network was created using the holdback method with a holdback proportion of 0.3333 and 3 hidden nodes which accept the initial variables and apply a

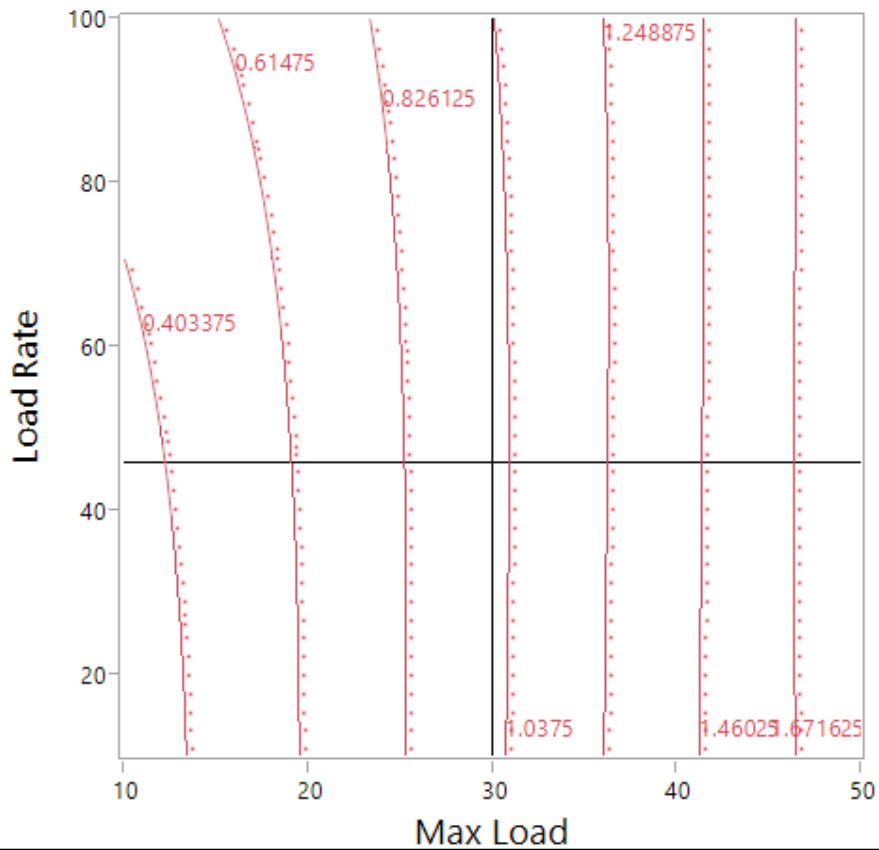


Figure 43: Contour plot of the displacement with respect to maximum load and load rate.

transfer function before combining the results. This divides the data randomly into two different sets; one set used to create the model and the second used to validate it to avoid overfitting of the data. This created an initial model of the data with an R^2 value of 0.9998. It was then validated at 0.9990, showing a better fit of the data than shown in the least squares analysis. This equation was developed between a maximum load of 10 to 50 kN and a maximum load rate of 10 to 100 kN. Impacts to the frontal or lateral regions use the appropriate value seen in their choice functions. Again, location should be treated as an ordinal parameter. The neural network equation can be seen in equation 9.

$$Deflection = -72.6897 - 19.8096 * H1 - 10.1052 * H2 + 374.1729 * H3;$$

$$H1 = TanH \left(0.5 * \left(0.4517 - 0.01578 * (Max Load) + 0.004198 \right. \right.$$

$$\left. * (Load Rate) - \left\{ \begin{array}{l} Frontal = 0 \\ Lateral = 0.03390 \end{array} \right\} \right)$$

$$H2 = TanH \left(0.5 * \left(4.9842 - 0.02376 * (Max Load) - 0.0006902 \right. \right.$$

$$\left. * (Load Rate) - \left\{ \begin{array}{l} Frontal = 0 \\ Lateral = 0.5780 \end{array} \right\} \right)$$

$$H3 = TanH \left(0.5 * \left(0.4739 - 0.0007084 * (Max Load) + 0.0002311 \right. \right.$$

$$\left. * (Load Rate) + \left\{ \begin{array}{l} Frontal = 0 \\ Lateral = 0.001328 \end{array} \right\} \right) \dots \dots \dots (9)$$

Inputs for maximum load are kN and inputs for maximum load rate are kN/ms.

Output is in units of millimeters. Effect testing for the model gives weights for the importance of variables in contributing to the overall effect. Maximum load had a relative

effect of 0.492, position had an effect of 0.006, and load rate had an effect of 0.002.

Though diminished compared to the maximum load, the effect of the load rate is still clearly visible in the contour plot of figure 43.

The lowest predicted value using the boundaries of the input parameters was at maximum load rate = 10 kN/ms, maximum load = 10 kN, and frontal analysis. This yielded a maximum deflection of 0.2820 mm, compared to the lowest recorded value of 0.2920 mm. This was more accurate than the least squares value by a factor of 9.75. A maximum predicted value at load = 50 kN, load rate = 100 kN/ms, lateral mode gave a prediction of 1.9806 mm compared to the observed 1.9830 mm. This also gave a more accurate result to the observed maximum when compared to least squares, by a factor of 11.67. The hump in the 50 kN test was not observed in the lateral mode. A plot of the displacements centered about the average point by load rate can be seen in figure 44. Though this does not show the same anomaly as in the stress calculation, where an increasing load rate caused a decreased von Mises development at large forces, the pattern of constantly decreasing effect of load rate on deflection is not seen. Careful examination of the graph shows that the sensitivity of the 30 kN trial mirrors that of the 50 kN test such that the 40 kN load series was more sensitive to the effects of the load rate. Given the small effects that load rate has shown to exhibit at large loads, this is likely a result of noise in the model. A plot of the residuals of the prediction equation to the fitted data is viewable in figure 45.

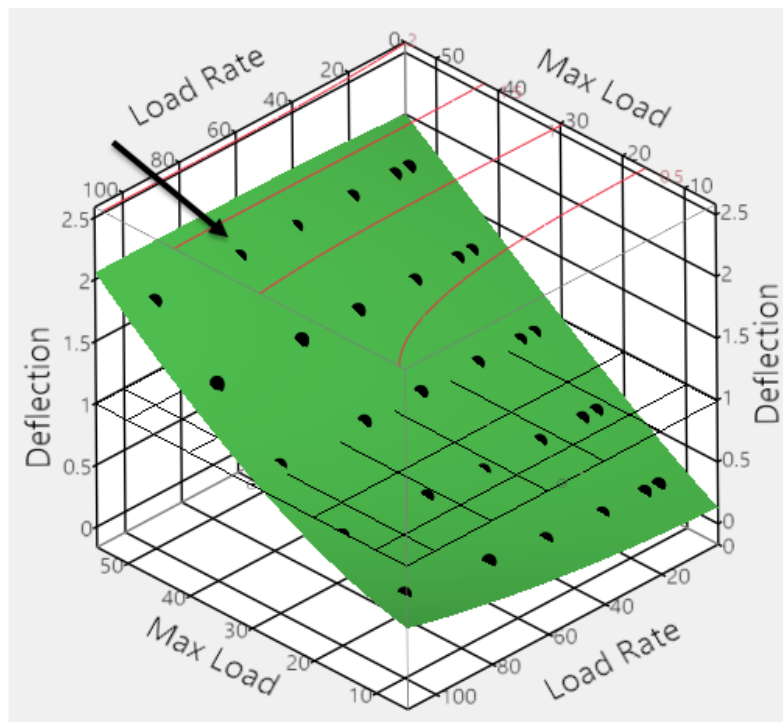
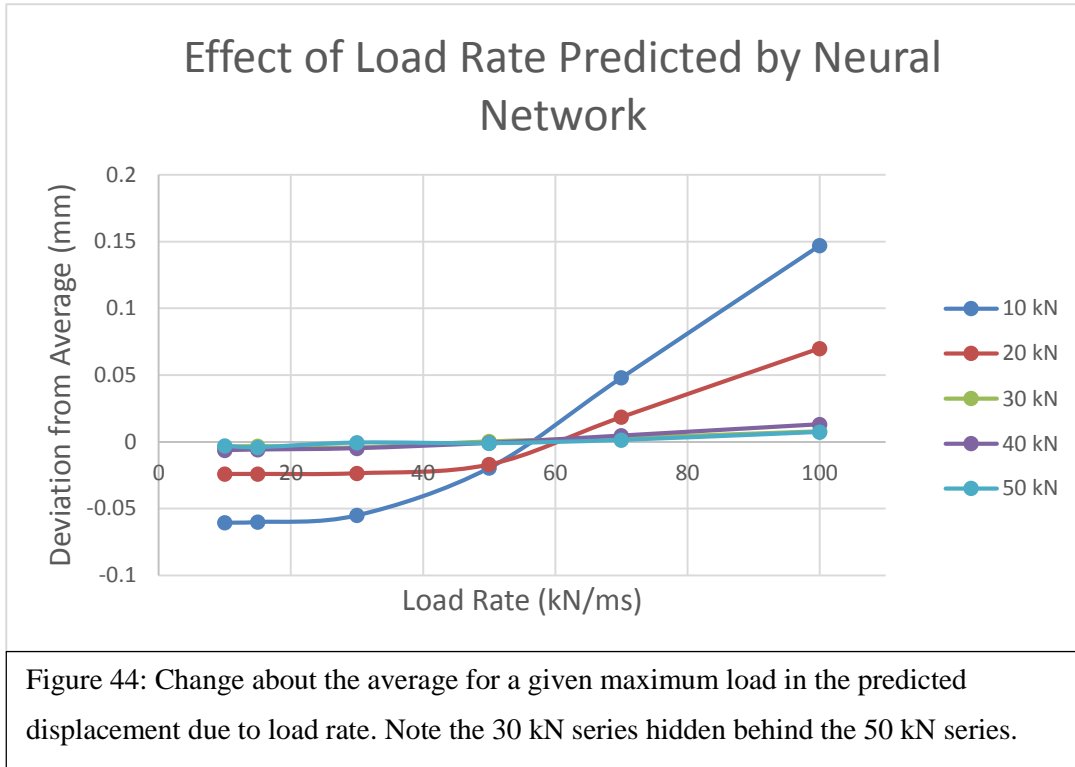


Figure 45: Plot of residuals of the neural network model. Contour lines can be seen on the top of the diagram.

6.14. Comparison of Results

Comparison of the values shown here can be made to the outcomes of falls published in O’Riordain.⁴⁴ Fall reconstruction in this paper revealed that force loading of at least 26 kN and 40 kN/ms were found to cause skull fracture. While the sample size for this study is limited, the corresponding von Mises value for these parameters using the neural network model is 46.6 MPa for the lateral section of the head and 40.9 for the frontal side. The deflections are 1.07 and 0.94 mm. This corresponds with measured values for the von Mises stress required to induce cranial fracture of 35 to 50 MPa.⁵³

The closeness of the stress values developed of the frontal and lateral simulations were found to match data found in literature. Assuming sphenoidal fracture as purely lateral, given that stress was found to accumulate in the region for lateral impacts, the proportion of frontal and lateral fractures was found to be approximately the same, with slightly more frontal fractures occurring than lateral.⁴⁸ This data had a low sample size however (n=40) and few studies have reported the exact frequency with which different locations of the head are struck during an impact. Given the data available, this result is supported. Lateral and frontal fracture thresholds were found to be relatively similar, with a 12% difference at the threshold fracture value (40.9 MPa for frontal and 46.6 for lateral). The further refined experimentation may uncover a difference in these values later.

Chapter 7: Conclusions

This study examined the biomechanics of skull injury due to forces experienced during fall scenarios by development of a finite element model. This model was formed using CT data of a healthy, adult male and validated for the frontal and lateral impact regions using prior laboratory studies. Fall data was then discretized from force deflection curves published previously. This data was transformed to simulate maximum loads and load rates that would be experienced in fall scenarios. Simulations were then run for each combination of location, load rate, and load. As could be expected, the highest maximum load and load rate showed the largest stress values. Fall force and load rate values that designated as a threshold for injury (26 kN and 40 kN/ms) were found by the finite element model to lie at the von Mises breaking stress for bone (40.9 MPa for frontal and 46.6 for lateral). This value was found to be larger in lateral impacts than in frontal ones. It follows that any collision where these loads are achieved has a large chance of causing some form of traumatic brain injury, with possible complications due to fracture.

The data presented here creates a new model for skull fracture prediction and two equations were created using a neural network to predict for stress and deflection values in the skull, both of which achieved R^2 values of 0.9990. By least squares analysis of data, maximum load, location, and load rate were found to be significant in the calculation of von Mises stress evoked in a collision. Additionally, the combination terms of (maximum

load)*(maximum load rate) and (maximum load)*(location) were found to be significant. This shows that the development of finite element models for the skull, which typically include purely elastic elements, only describes part of the response of an impact.

Future work needs to be done in several areas to generate a more complete and accurate model. Location parameters need to be formed into a continuum to predict injury rates around the entire head. Additionally, the area of impact should be varied to measure its influence on the model. Additional research outside of computer simulations into the rate, frequency, striking material composition, and forces generated by of sub-injurious falls should also be done to generate a more complete risk assessment for falls and similar injury modes.

Chapter 8: References

1. Adams, J. H., D. Doyle, I. Ford, T. Gennarelli, D. Graham, and D. McLellan. Diffuse axonal injury in head injury: definition, diagnosis and grading. *Histopathology* 15:49-59, 1989.
2. Adams, J. H., D. Graham, L. S. Murray, and G. Scott. Diffuse axonal injury due to nonmissile head injury in humans: an analysis of 45 cases. *Ann. Neurol.* 12:557-563, 1982.
3. Allsop, D. L., T. R. Perl, and C. Y. Warner. Force/Deflection and Fracture Characteristics of the Temporor-Parietal Region of the Human Head. *SAE transactions* 100:2009-2009, 1992.
4. Annegers, J. F. and S. P. Coan. The risks of epilepsy after traumatic brain injury. *Seizure* 9:453-457, 2000.
5. Arundine, M., M. Aarts, A. Lau, and M. Tymianski. Vulnerability of central neurons to secondary insults after in vitro mechanical stretch. *The Journal of neuroscience* 24:8106-8123, 2004.
6. Bain, A. C. and D. F. Meaney. Tissue-level thresholds for axonal damage in an experimental model of central nervous system white matter injury. *J. Biomech. Eng.* 122:615-622, 2000.
7. Bayly, P., T. Cohen, E. Leister, D. Ajo, E. Leuthardt, and G. Genin. Deformation of the human brain induced by mild acceleration. *J. Neurotrauma* 22:845-856, 2005.

8. Bazarian, J. J., J. Mcclung, M. N. Shah, Y. Ting Cheng, W. Flesher, and J. Kraus. Mild traumatic brain injury in the United States, 1998-2000. *Brain Injury* 19:85-91, 2005.
9. Bruns, J. and W. A. Hauser. The epidemiology of traumatic brain injury: a review. *Epilepsia* 44:2-10, 2003.
10. Cormier, J., S. Manoogian, J. Bisplinghoff, S. Rowson, A. Santago, C. McNally, S. Duma, and J. Bolte IV. The tolerance of the frontal bone to blunt impact. *J. Biomech. Eng.* 133, 2011.
11. Coronado, V. G., M. Faul, M. M. Wald, and L. Xu. Traumatic brain injury in the United States: emergency department visits, hospitalizations, and deaths, 2002-2006. : Department of Health and Human Services, Centers for Disease Control and Prevention, National Center for Injury Prevention and Control, 2010.
12. Crisco, J. J., R. Fiore, J. G. Beckwith, J. J. Chu, P. G. Brolinson, S. Duma, T. W. McAllister, A. C. Duhaime, and R. M. Greenwald. Frequency and location of head impact exposures in individual collegiate football players. *J. Athl Train.* 45:549-559, 2010.
13. Drabousky, D. P. Prony series representation and interconversion of viscoelastic material functions of equine cortical bone. Cleveland; Case Western Reserve University, 2009, 193p.

14. Feng, Y., T. Abney, R. Okamoto, R. Pless, G. Genin, and P. V. Bayly. Relative brain displacement and deformation during constrained mild frontal head impact. *Journal of The Royal Society Interface* 7:1677-1688, 2010.
15. Foda, M. and A. Marmarou. A new model of diffuse brain injury in rats: Part II: Morphological characterization. *J. Neurosurg.* 80:301-313, 1994.
16. Forbes, J. A., T. J. Withrow, B. Erwin Yap, A. A. Abla, J. S. Cheng, R. Thompson, and A. Sills. Biomechanics of Subdural Hemorrhage in American Football. Department of Neurological Surgery, Vanderbilt University Medical Center. Nashville, TN , 2010.
17. Galarneau, M. R., S. I. Woodruff, J. L. Dye, C. R. Mohrle, and A. L. Wade. Traumatic brain injury during Operation Iraqi Freedom: findings from the United States Navy–Marine Corps Combat Trauma Registry. *J. Neurosurg* 108:950-957, 2008.
18. Gennarelli, T., L. Thibault, G. Tomei, R. Wiser, and D. Graham. Directional dependence of axonal brain injury due to centroidal and non-centroidal acceleration. *SAE Technical Paper*, 1987.
19. Gennarelli, T. A., H. R. Champion, W. S. Copes, and W. J. Sacco. Comparison of mortality, morbidity, and severity of 59,713 head injured patients with 114,447 patients with extracranial injuries. *Journal of Trauma-Injury, Infection, and Critical Care* 37:962-968, 1994.
20. Graham, D., J. Clark, J. Adams, and T. Gennarelli. Diffuse axonal injury caused by assault. *J. Clin. Pathol.* 45:840-841, 1992.

21. Gurdjian, E., J. E. Webster, and H. Lissner. The mechanism of skull fracture. *J. Neurosurg.* 7:106-114, 1950.
22. Harrigan, T., J. Roberts, E. Ward, and A. Merkle. Correlating Tissue Response with Anatomical Location of mTBI Using a Human Head Finite Element Model under Simulated Blast Conditions. *IFMBE Proceedings*:18-21, 2010.
23. Hodgson, V. R. Tolerance of the facial bones to impact. *Am. J. Anat.* 120:113-122, 1967.
24. Hodgson, V. R., J. Brinn, L. Thomas, and S. Greenberg. Fracture behavior of the skull frontal bone against cylindrical surfaces. *Development* 2010:04-13, 1970.
25. Hodgson, V., L. Thomas, and T. Khalil. The role of impact location in reversible cerebral concussion. *SAE Technical Papers*, 1983.
26. Hofman, P. A., P. Nelemans, G. J. Kemerink, and J. T. Wilmink. Value of radiological diagnosis of skull fracture in the management of mild head injury: meta-analysis. *J. Neurol. Neurosurg. Psychiatry.* 68:416-422, 2000.
27. Holcomb, J. B., L. G. Stansbury, H. R. Champion, C. Wade, and R. F. Bellamy. Understanding combat casualty care statistics. *J. Trauma* 60:397-401, 2006.
28. Hosey, R. R. and Y. K. Liu. A homeomorphic finite element model of the human head and neck. *Finite elements in biomechanics* 3:379-401, 1982.
29. Jaslow, C. R. Mechanical properties of cranial sutures. *J. Biomech.* 23:313-321, 1990.

30. Kleiven, S. Influence of impact direction on the human head in prediction of subdural hematoma. *J. Neurotrauma* 20:365-379, 2003.
31. Kremer, C., S. Racette, C. Dionne, and A. Sauvageau. Discrimination of falls and blows in blunt head trauma: systematic study of the hat brim line rule in relation to skull fractures. *J. Forensic Sci.* 53:716-719, 2008.
32. Lamy, M., D. Baumgartner, N. Yoganandan, B. D. Stemper, and R. Willinger. Experimentally validated three-dimensional finite element model of the rat for mild traumatic brain injury. *Med. Biol. Eng. Comput.* 51:1-13, 2013.
33. Lighthall, J. W. Controlled cortical impact: a new experimental brain injury model. *J. Neurotrauma* 5:1-15, 1988.
34. Ling, G., F. Bandak, R. Armonda, G. Grant, and J. Ecklund. Explosive blast neurotrauma. *J. Neurotrauma* 26:815-825, 2009.
35. Löwenhielm, P. Mathematical simulation of gliding contusions. *J. Biomech.* 8:351-356, 1975.
36. Mac Donald, C. L., A. M. Johnson, D. Cooper, E. C. Nelson, N. J. Werner, J. S. Shimony, A. Z. Snyder, M. E. Raichle, J. R. Witherow, and R. Fang. Detection of blast-related traumatic brain injury in US military personnel. *N. Engl. J. Med.* 364:2091-2100, 2011.
37. Margulies, S. S. and L. E. Thibault. A proposed tolerance criterion for diffuse axonal injury in man. *J. Biomech.* 25:917-923, 1992.

38. Marjoux, D., D. Baumgartner, C. Deck, and R. Willinger. Head injury prediction capability of the HIC, HIP, SIMon and ULP criteria. *Accident Analysis & Prevention* 40:1135-1148, 2008.
39. Meythaler, J. M., J. D. Peduzzi, E. Eleftheriou, and T. A. Novack. Current concepts: Diffuse axonal injury [ndash] associated traumatic brain injury. *Arch. Phys. Med. Rehabil.* 82:1461-1471, 2001.
40. Moss, W. C., M. J. King, and E. G. Blackman. Skull flexure from blast waves: a mechanism for brain injury with implications for helmet design. *Phys. Rev. Lett.* 103:108702, 2009.
41. Nahum, A. M., J. D. Gatts, and C. W. Gadd. Impact tolerance of the skull and face. , 1968.
42. Newman, J. A. Head Injury Criteria in Automotive Crash Testing. SAE Technical Paper , 1980.
43. Norton, M. R. and C. Gamble. Bone classification: an objective scale of bone density using the computerized tomography scan. *Clin. Oral Implants Res.* 12:79-84, 2001.
44. O’Riordain, K., P. M. Thomas, J. P. Phillips, and M. D. Gilchrist. Reconstruction of real world head injury accidents resulting from falls using multibody dynamics. *Clin. Biomech.* 18:590-600, 2003.

45. Ommaya, A. K., editor. Head and Neck Injury Criteria: A Consensus Workshop. Washington DC: U.S. Department of Transportation, National Highway Traffic Safety Administration, 1981.
46. Ommaya, A. K., A. E. Hirsch, P. Yarnell, and E. H. Harris. Scaling of experimental data on cerebral concussion in sub-human primates to concussion threshold for man. SAE Technical Paper, 1967.
47. Panzer, M. B., B. S. Myers, B. P. Capehart, and C. R. Bass. Development of a finite element model for blast brain injury and the effects of CSF cavitation. *Ann. Biomed. Eng.* 40:1530-1544, 2012.
48. Pappachan, B. and M. Alexander. Correlating Facial Fractures and Cranial Injuries. *Journal of Oral and Maxillofacial Surgery* 64:1023-1029, 2006.
49. Patel, A. and T. Goswami. "Comparison of Intracranial Pressure by Lateral and Frontal Impacts – Validation of Computational Model." In: *Injury and Skeletal Biomechanics*, edited by T. Goswami. InTech, 2012, pp. 95-114.
50. Petr, K., M. W. Bondi, S. R. Ward, and L. R. Frank. On sources of error in finite element simulations of blast effects in the human brain. *Journal of computational and nonlinear dynamics* 7, 2012.
51. Raul, J., D. Baumgartner, R. Willinger, and B. Ludes. Finite element modelling of human head injuries caused by a fall. *Int. J. Legal Med.* 120:212-218, 2006.

52. Smith, D., X. Chen, B. Xu, T. McIntosh, T. Gennarelli, and D. Meaney. Characterization of diffuse axonal pathology and selective hippocampal damage following inertial brain trauma in the pig. *J. Neuropathol. Exp. Neurol.* 56:822-834, 1997.
53. Soltesz, U. and H. Richter. Mechanical behavior of selected ceramics. *Metal and ceramic biomaterials* 2:24, 1984.
54. Stevens, J. A. and N. Adekoya. Brain injury resulting from falls among elderly persons. *JAMA: The Journal of the American Medical Association* 286:2665-2666, 2001.
55. Swearingen, J. J. Tolerances of the human face to crash impact. : Federal Aviation Agency, Office of Aviation Medicine, Civil Aeromedical Research Institute, 1965.
56. Takhounts, E. G., S. A. Ridella, V. Hasija, R. E. Tannous, J. Q. Campbell, D. Malone, K. Danelson, J. Stitzel, S. Rowson, and S. Duma. Investigation of traumatic brain injuries using the next generation of simulated injury monitor (SIMon) finite element head model. *Stapp Car Crash J* 52:1-31, 2008.
57. Tse, K. M., L. B. Tan, S. J. Lee, S. P. Lim, and H. P. Lee. A Realistic Subject-Specific Finite Element Model of Human Head-Development and Experimental Validation. *The 15th International Conference on Biomedical Engineering*. Springer International Publishing, 2014.
58. Voigt, G. E. and K. Wilfert. Mechanisms of injuries to unrestrained drivers in head-on collisions. *SAE Technical Paper*, 1969.

59. Willinger, R., H. S. Kang, and B. Diaw. Three-dimensional human head finite-element model validation against two experimental impacts. *Ann. Biomed. Eng.* 27:403-410, 1999.
60. Yoganandan, N. and F. A. Pintar. Biomechanics of temporo-parietal skull fracture. *Clin. Biomech.* 19:225-239, 2004.
61. Yoganandan, N., F. A. Pintar, A. Sances Jr, P. R. Walsh, C. L. Ewing, D. J. Thomas, and R. G. Snyder. Biomechanics of skull fracture. *J. Neurotrauma* 12:659-668, 1995.
62. Yoganandan, N., A. Sances Jr, F. A. Pintar, D. J. Maiman, D. C. Hemmy, S. J. Larson, and V. M. Haughton. Traumatic facial injuries with steering wheel loading. *Journal of Trauma-Injury, Infection, and Critical Care* 31:699-710, 1991.
63. Zhang, L., K. H. Yang, A. I. King, and D. Viano. A new biomechanical predictor for mild traumatic brain injury—A preliminary finding. *Proc. 2003 Summer Bioengineering Conference.* 137-138, 2003.
64. Zhang, L., K. H. Yang, and A. I. King. Comparison of brain responses between frontal and lateral impacts by finite element modeling. *J. Neurotrauma* 18:21-30, 2001.
65. Zukas, J. A. and D. R. Scheffler. Practical aspects of numerical simulations of dynamic events: effects of meshing. *Int. J. Impact Eng.* 24:925-945, 2000.